



National
Defence Défense
nationale



THE EFFECTS OF THE ENVIRONMENT ON AN EXPERIMENTAL VHF RADIO DIRECTION FINDING ANTENNA SYSTEM

by

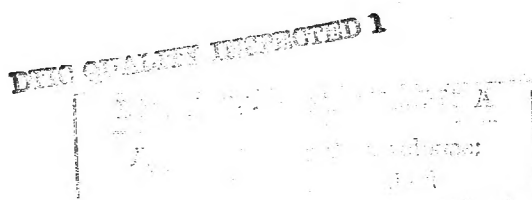
William Read



19941214 040

DEFENCE RESEARCH ESTABLISHMENT OTTAWA
REPORT NO. 1226

Canada



**August 1994
Ottawa**



National
Defence

Défense
nationale

THE EFFECTS OF THE ENVIRONMENT ON AN EXPERIMENTAL VHF RADIO DIRECTION FINDING ANTENNA SYSTEM

by

William Read
Electronic Support Measures Section
Electronic Warfare Division

Accession For	
NTIS	CRA&I
DTIC	TAB
Unannounced	
Justification _____	
By _____	
Distribution _____	
Availability Codes	
Dist	Avail and/or Special
A-1	

DEFENCE RESEARCH ESTABLISHMENT OTTAWA
REPORT NO. 1226

PCN
041LX

August 1994
Ottawa

ABSTRACT

This report discusses the results of VHF radio direction finding (DF) experiments carried out with an experimental linear eight-antenna DF system. The main purpose of these experiments was to investigate the effect of the environment, in particular multipath propagation, on DF performance. A theoretical analysis of all known error mechanisms has also been carried out in order to better understand the measured results. This includes temporal noise, equipment errors, mutual coupling, and multipath. The analysis of multipath also includes the development of new models to predict statistical effects. The results of this investigation indicate that multipath effects are complex and may create difficulties in modern systems if improved accuracy is an objective. Further measurements will be required to verify these preliminary findings.

RÉSUMÉ

Ce rapport traite des résultats expérimentaux issus de tests réalisés à l'aide d'un système expérimental de radiogoniométrie à huit antennes VHF réparties linéairement. L'objectif principal poursuivi lors de ces tests était d'étudier les effets environnementaux sur les performances des mesures radiogoniométriques et, plus particulièrement, l'effet des propagations multi-voies. Afin d'obtenir une meilleure compréhension des résultats mesurés, une analyse théorique de tous les types connus de mécanismes d'erreur a été menée, incluant les erreurs dues aux bruits variant dans le temps, aux problèmes d'équipement, à l'effet de couplage mutuel et, enfin, aux propagations multi-voies. L'analyse des propagations multi-voies comprend également le développement de nouveaux modèles visant à prédire les effets statistiques. Les résultats de ces recherches indiquent que les effets des propagations multi-voies s'avèrent d'une grande complexité et causeront probablement certains problèmes aux systèmes modernes radiogoniométriques cherchant à améliorer la précision des mesures. Ces résultats préliminaires devront toutefois être vérifiés par des tests et mesures supplémentaires.

EXECUTIVE SUMMARY

Improvement of communications radio direction finding (DF) accuracy is a high priority for the Canadian and Allied Forces. To this end, research in advanced DF techniques has been carried out worldwide over the last two decades with the view of taking advantage of advances in DF algorithms as well as the capabilities of modern processing technology. At the Defence Research Establishment Ottawa (DREO), an experimental eight-channel VHF DF system, called the Osprey System, has been set up to investigate the distortion of the received signal wavefront caused by multipath propagation. Field trials with this system took place in the Fall of 1992 and the Spring of 1993. These trials were carried out in support of the Canadian Forces for the improvement of land tactical VHF/UHF DF accuracy, and in support of TTCP QTP-18 to investigate environmental effects on a VHF DF system.

This report discusses and analyzes the results of these field trials. The theoretical effects of error mechanisms which degraded the DF measurements are analyzed in detail, including the modelling of the multipath environment. This analysis is then used to break down the measured errors in terms of these mechanisms. The effects due to each mechanism are then studied in more detail.

Quantitatively, multipath propagation was found to be the greatest source of error. It was followed closely by mutual coupling. Based on the modelling studies of both phenomena, important qualitative differences were found. Mutual coupling errors are a function of transmitter azimuth only (when a plane wave signal is considered) and are predictable. The error pattern changes relatively slowly; cycling once from the maximum positive error to the maximum negative error over a range of 180 degrees in azimuth. Multipath errors are a function of both transmitter azimuth and range. The error pattern becomes more unpredictable (noise-like) as the range of the multipath source from the DF system increases (at a range of 0 meters multipath and mutual coupling can be regarded as the same phenomena). These qualitative differences make it relatively easy to distinguish mutual coupling effects from multipath effects.

In examining the actual multipath induced errors, two important observations were made. The first was that the multipath errors were very noise-like indicating significant sources of multipath at ranges of several hundred meters or more. The second was that there appears to be a transmitter range dependency even for transmitter ranges over 5 km. Based on the theoretical models, this implies that sources of multipath which are reflective in nature (i.e. redirect the incident signal in a new direction with limited scattering) are significant. Both observations lead to complications for site calibration

if improved DF accuracy is the objective. They indicate that calibration of the array steering vector (or array manifold) at a particular frequency needs to be performed as a function of both range and azimuth, not azimuth as is usually done. Further experimentation will be required to verify these observations before any definite conclusions can be drawn.

In general the results described in this report indicate that the multipath environment is very complex. Modelling can be used, with some success, to better understand the statistical effects of multipath. For future work, the theoretical models need to be refined to better approximate real life effects. Further field testing will also be required to verify these models and determine appropriate model parameters (e.g. density of multipath sources, relative importance of reflective versus scattering types, etc.). This could ultimately lead to the development of new approaches to VHF DF including (but not restricted to) new algorithms and new calibration techniques.

TABLE OF CONTENTS

ABSTRACT/RÉSUMÉ	iii
EXECUTIVE SUMMARY	v
TABLE OF CONTENTS	vii
LIST OF FIGURES	ix
LIST OF TABLES	xi
1.0 INTRODUCTION	1
2.0 EXPERIMENTAL SETUP	2
2.1 Site Layout	2
2.2 Acquisition System	3
2.3 The Test Plan	4
3.0 SIGNAL PROCESSING CONSIDERATIONS	10
3.1 IQ Conversion	10
3.2 Channel Equalization	12
3.3 The MUSIC DF Algorithm	14
4.0 SOURCES OF ERROR	15
4.1 Transmitter Position	15
4.2 Noise	16
4.3 Wind Effects	20
4.4 Mutual Coupling	22
4.5 Multipath	28
4.5.1 Freespace model	29
4.5.2 Plane Earth Model	31
4.5.3 Multipath Model	34
5.0 RESULTS	48
5.1 Error Analysis	48
5.1.1 Temporal Effects	53
5.1.2 Spatial Effects	60
5.1.3 Multipath Effects	61
6.0 CONCLUSIONS	68
REFERENCES	REF-1
A.0 Stochastic Calibration Method	A-1

LIST OF FIGURES

Figure 1: Experimental N channel DF system block diagram.	1
Figure 2: Physical layout of field trial DF site.	3
Figure 3: Transmitter locations on November 5, 1992	6
Figure 4: Transmitter locations on November 6, 1992	7
Figure 5: Transmitter locations on March 24, 1993	8
Figure 6: Transmitter locations on March 25, 1993	9
Figure 7: FFT spectrum of raw baseband data from channel 0	10
Figure 8: Theoretical absolute mean bearing error (a) and bearing variance (b) of the Osprey System as a function of signal bearing and SNR.	19
Figure 9: Equivalent electrical circuit for antenna 0.	23
Figure 10: Estimated bearing versus true bearings with mutual coupling.	26
Figure 11: Mutual coupling bearing errors	27
Figure 12: Effective collecting area of an isotropic antenna.	30
Figure 13: Plane Earth propagation model.	31
Figure 14: Reflection coefficient versus grazing angle.	32
Figure 15: Plane Earth propagation model for a perfect reflector.	35
Figure 16: Excess path loss for a perfect reflector.	37
Figure 17: Plane Earth propagation model for an isotropic scatterer.	38
Figure 18: Excess path loss for an isotropic scatterer.	40
Figure 19: Directional multipath power loss l_φ	42
Figure 20: Combined effect of excess path loss and directional loss for a perfect reflector.	44

Figure 21: Combined effect of excess path loss and directional loss for an isotropic scatterer.	45
Figure 22: Simulated DF error response for 3 multipath reflectors	46
Figure 23: Simulated DF error response for 3 multipath scatterers	47
Figure 24: Field trial results for November 5, 1992	49
Figure 25: Field trial results for November 6, 1992	50
Figure 26: Field trial results for March 24, 1993	51
Figure 27: Field trial results for March 25, 1993	52
Figure 28: Field trial parameters for November 5, 1992	54
Figure 29: Field trial parameters for November 6, 1992	55
Figure 30: Field trial parameters for March 24, 1993	56
Figure 31: Field trial parameters for March 25, 1993	57
Figure 32: Theoretical mutual coupling effects compared to results from March 25, 1993	62
Figure 33: Revised error results for November 5, 1992.	63
Figure 34: Revised error results for November 6, 1992.	64
Figure 35: Revised error results for March 24, 1993.	65
Figure 36: Revised error results for March 25, 1993.	66

LIST OF TABLES

Table 1: RMS Error Summary of Field Trial Results	48
Table 2: Data Subsets for Drift Estimation	58
Table 3: Channel Phase Drift during Field Trials in November	59
Table 4: Channel Phase and Gain Drift during Field Trials in March	59
Table 5: Bearing Errors due to Phase and Gain Drift	60
Table 6: Simulated Bearing Errors due to Mutual Coupling	61
Table 7: RMS Error Summary of Field Trial Results with Mutual Coupling Effects Removed	67
Table 8: RMS Error Summary	69

1.0 INTRODUCTION

Improvement of communications radio direction finding (DF) accuracy is a high priority for the Canadian and Allied Forces. To this end, research in advanced DF techniques has been carried out worldwide over the last two decades with the view of taking advantage of advances in DF algorithms as well as the capabilities of modern processing technology. Central to this approach is the N -channel digital beamformer, one possible version of which is shown in block diagram form in Figure 1. The main advantage of this approach is that the phase and amplitude measurements from each antenna are available for analysis. This maximizes the information available about the incoming radio signal which allows multiple signal DF (superresolution) to be performed, or distortion of the received wavefront (compared to theoretical expectations) to be measured.

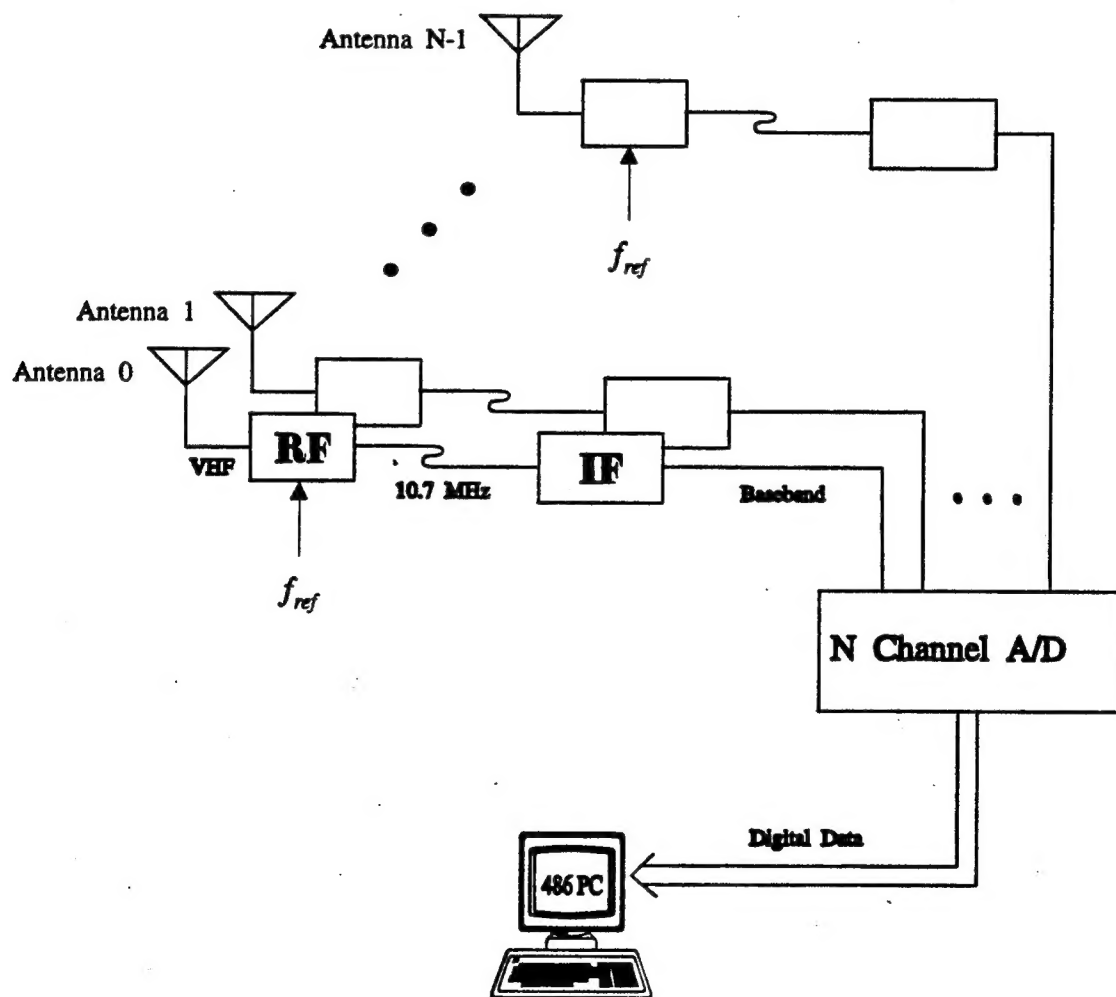


Figure 1: Experimental N channel DF system block diagram.

At DREO an eight-channel hardware realization of Figure 1, called the Osprey System, has been set up to investigate the distortion of the received signal waveform caused by multipath propagation. This report describes and analyzes the results of VHF DF field trials which took place during the Fall of 1992 and the Spring of 1993. The trials were carried out in support of the Canadian Forces for the improvement of land tactical VHF/UHF DF accuracy, and in support of TTCP QTP-18 to investigate environmental effects on a VHF DF system.

This report is arranged in six main sections. The first section is this introduction. Section 2 describes the experimental setup including a description of the site surrounding the Osprey System, the transmit and receive hardware, and the measurement test plan. Section 3 describes the processing of the data from conversion to IQ format to the calculation of the transmitter signal bearing. Section 4 provides a theoretical evaluation of the sources of error including the development of multipath models for the assessment of the effects of multipath on DF. Section 5 describes the results in terms of the error sources with the objective of quantifying and qualifying the effects of multipath. Finally the conclusions are presented in Section 6.

To avoid ambiguities, the following definitions for antenna systems have been used in this report:

Antenna A structure which collects electromagnetic energy and converts it into electrical energy. It has a single output which is connected to a single receiver channel.

Antenna Element A part of the antenna structure, e.g. a vertical dipole antenna has an upper element and a lower element.

Antenna Array A collection of N antennas which are connected to N receiver channels.

Note that these definitions do not necessarily reflect the most common usage of these terms. They have been defined in a way that is most appropriate for this report.

2.0 EXPERIMENTAL SETUP

2.1 Site Layout

The layout of the site was as shown in Figure 2. This was neither flat nor cleared of obstacles, but rather a site located on a flat field at DREO surrounded by trees, low wire fences, roads, a ditch, etc. In short, a variety of obstacles that according to [1] can cause errors in bearing measurements but are typical of the Ottawa area.

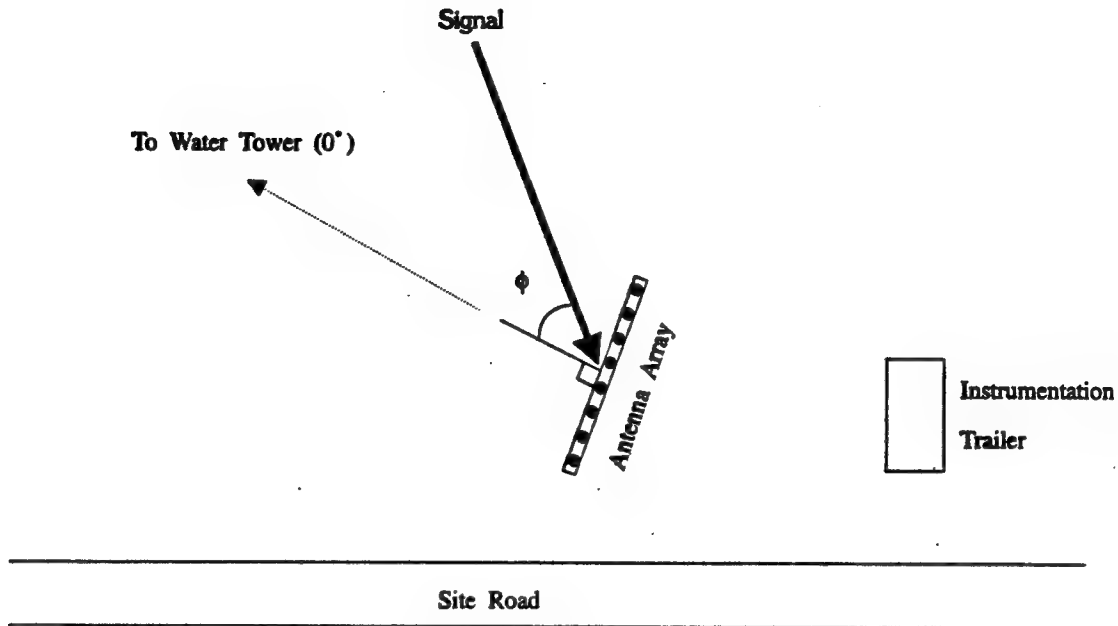


Figure 2: Physical layout of field trial DF site.

The Osprey antenna system consisted of a linear array of 2.9 meter dipole whip antennas spaced at intervals of 2 meters. The antennas were mounted on a 15 meter long fiberglass truss. The truss was in turn supported 2 meters off the ground by a large pivot at the center, enabling the truss to be rotated manually through 360 degrees. Adjustable supports at either end of the truss were used to prevent sagging over the length of the truss. For the experiments discussed in this report, the truss was left in the position shown in Figure 2 and the 0 degree azimuth bearing reference was also as shown.

For alignment purposes, the 0 degree bearing reference was chosen to correspond to the bearing of a water tower located at a range of 990 meters from the antenna system (not shown in Figure 2) which provided a useful map and visual marker. The alignment accuracy was assessed to be ± 1 degree.

2.2 Acquisition System

The data acquisition system shown in Figure 1 was designed for operation in the 30-100 MHz band. Each receiver consists of two parts: an RF front end mounted at the base of the antenna to downconvert the signal to 10.7 MHz, and a rack mounted IF unit located in the acquisition trailer to downconvert the 10.7 MHz signal to baseband. A common reference signal was used to control the input RF frequency of the front end units. Given its design, there were actually two input frequency bands, namely, $f_{ref} - 10.7$ MHz and

$f_{ref} + 10.7$ MHz where f_{ref} was the frequency of the reference signal. For the experiments, the reference frequencies $f_{ref} = 70$ MHz and $f_{ref} = 51.8$ MHz were used in the Fall and Spring respectively. To eliminate one of the input frequency bands, 55-67 MHz band pass filters were used at the input of the RF units. These filters also eliminate strong signals in the FM band which would have otherwise resulted in the generation of a high level of intermodulation noise in the receivers.

A digitally controlled attenuator in each receiver was used to adjust the IF gain. The attenuator settings were controlled by the A/D which was in turn controlled by a 486 PC. During the experiments the attenuators were left in the 0 dB setting, since changing the attenuator settings was found to affect the relative phase offsets between channels.

Receiver tuning was controlled through a single common synthesizer which is currently manually controlled but can be modified for computer control. The baseband output of the receivers is low pass filtered with an effective noise bandwidth of 7.1 kHz. This output is fed to the A/D converter which synchronously samples from one to eight channels. The digital output data is stored on the PC where it can be further processed. The channels sampled, sampling rate, and data blocksize are all computer controlled. For the experiments all eight channels were recorded at a sampling rate of 1.0 kHz. The blocksize was also limited to 2048 samples for each measurement to minimize the amount of data that required storage.

For the field trials, the transmitter equipment was placed in a Dodge minivan and a 2 meter monopole transmitting antenna attached to the roof of the vehicle. The transmitter equipment consisted of a synthesizer and power amplifier capable of generating a CW signal of up to 3 watts of power.

2.3 The Test Plan

The field trials consisted of four days of data collection which were the 5th and 6th of November 1992 and the 24th and 25th of March 1993. The routes followed on these days are shown in Figures 3-6. For each trial the transmitter was positioned at the start of the route until a DF measurement (or measurements) was taken, then moved 50 meters along the route to the next position for the next measurement. This was repeated until the whole route was covered. Moving the transmitter and taking a DF measurement generally took about 30 seconds.

For logistical reasons the chosen routes followed local roads, and the transmitter was always positioned on the right side of the road relative to the direction of travel. In a number of cases the routes, or parts of the routes, were repeated on the same or following day to investigate changes in the measurements over time.

The start position for each route was chosen to be easy to locate on a 1:25000 topographical map of the Ottawa area or a 1:5000 overhead photograph of the DREO site. Distance from the start position was measured using a fifth wheel (a bicycle wheel mounted on the back bumper of the vehicle which measures distance travelled) whose smallest measurement increment was 10 meters.

On the 5th of November and the 24th of March, one DF measurement was taken for each transmitter position. On the 6th of November two consecutive measurements were taken at a time. The objective was to determine the repeatability of the measurements for each transmitter position. Unfortunately, due to synchronization problems the transmitter was sometimes moving during the second measurement. When this happened the second measurement was discarded. On the 25th of March three consecutive DF measurements were taken at a time. Again, due to synchronization problems, some of these measurements had to be discarded.

The transmitter frequencies used were 59.3 MHz during the November trials, and 62.5 MHz during the March trials. Slight adjustments to these frequencies were made to ensure the final baseband frequency of the received signal of the Osprey System was between 150 Hz and 500 Hz.

During the November trials the temperatures were relatively constant and remained at about 2° C, the sky was overcast, and the ground was wet. During the March trials the temperatures ranged from 0° C in the morning to +7° C in the afternoon, the sky was clear, and the ground was frozen and snow covered to a depth of 50 cm.

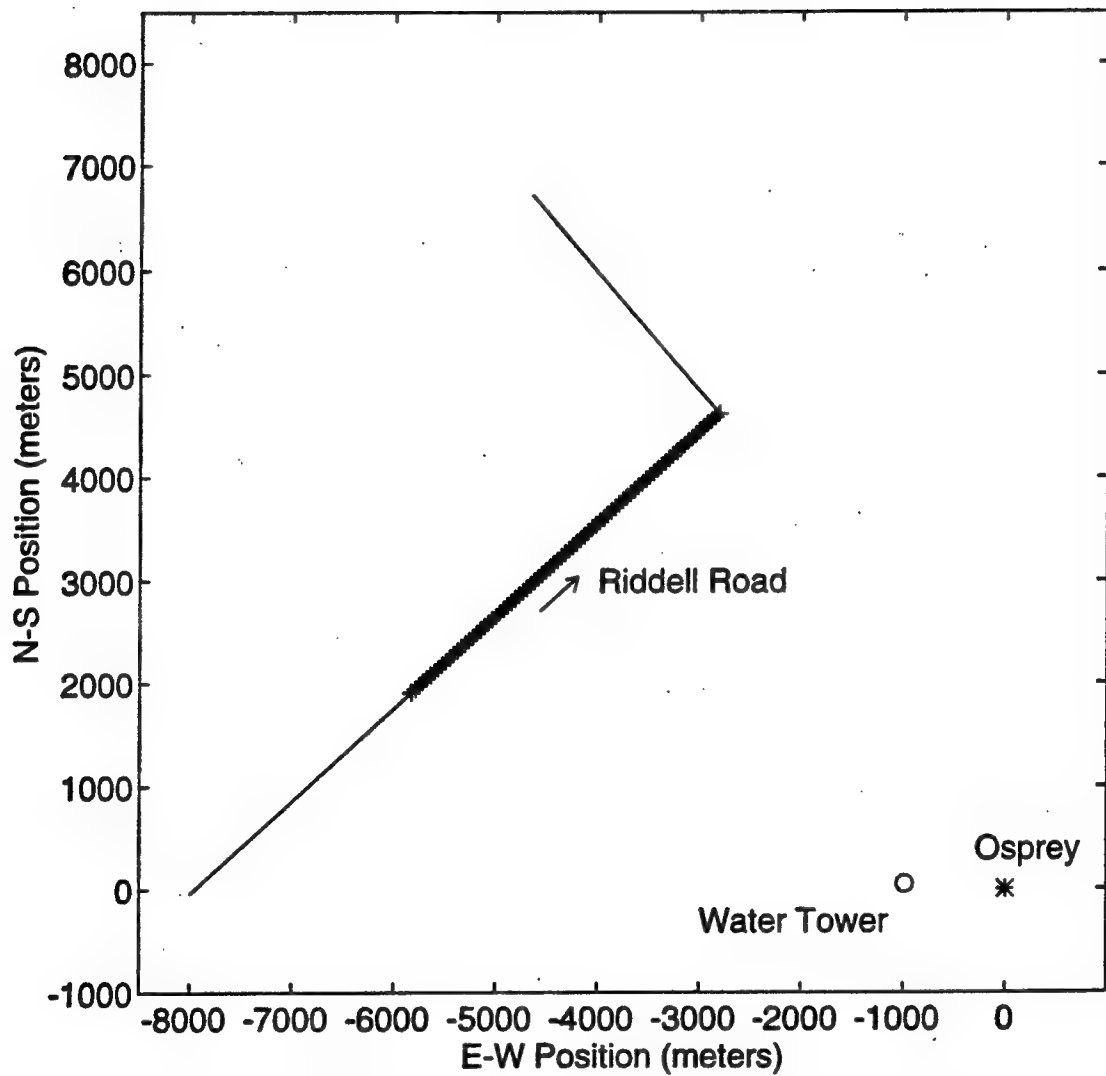


Figure 3: Transmitter locations (marked by +) on November 5, 1992 relative to Osprey system at (0,0). Arrows show vehicle direction. Start position was $(x_{E-W}, y_{N-S}) = (-5825, 1909)$

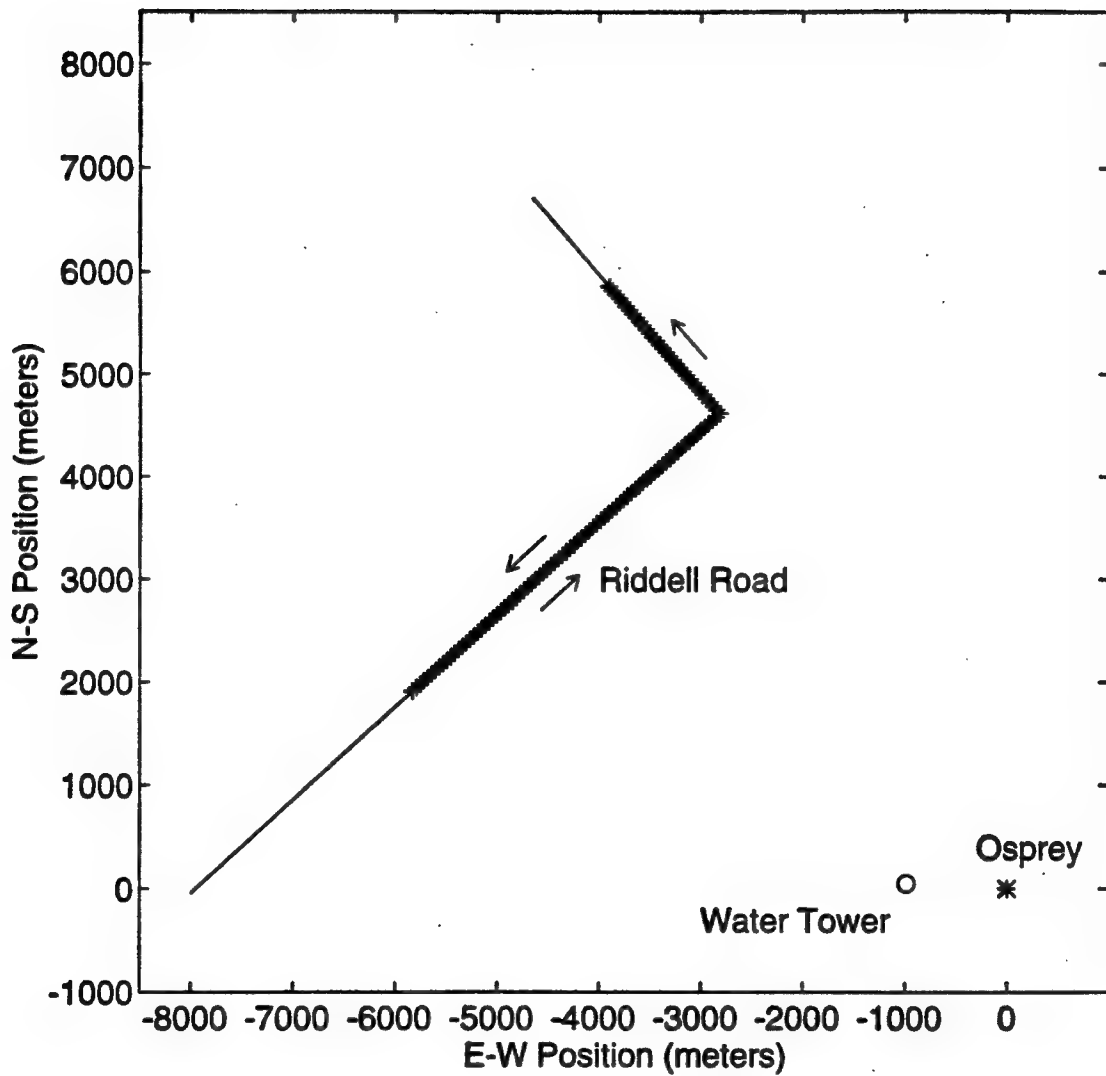


Figure 4: Transmitter locations (marked by +) on November 6, 1992 relative to Osprey system. Arrows show vehicle direction. Start position was $(x_{E-W}, y_{N-S}) = (-5825, 1909)$

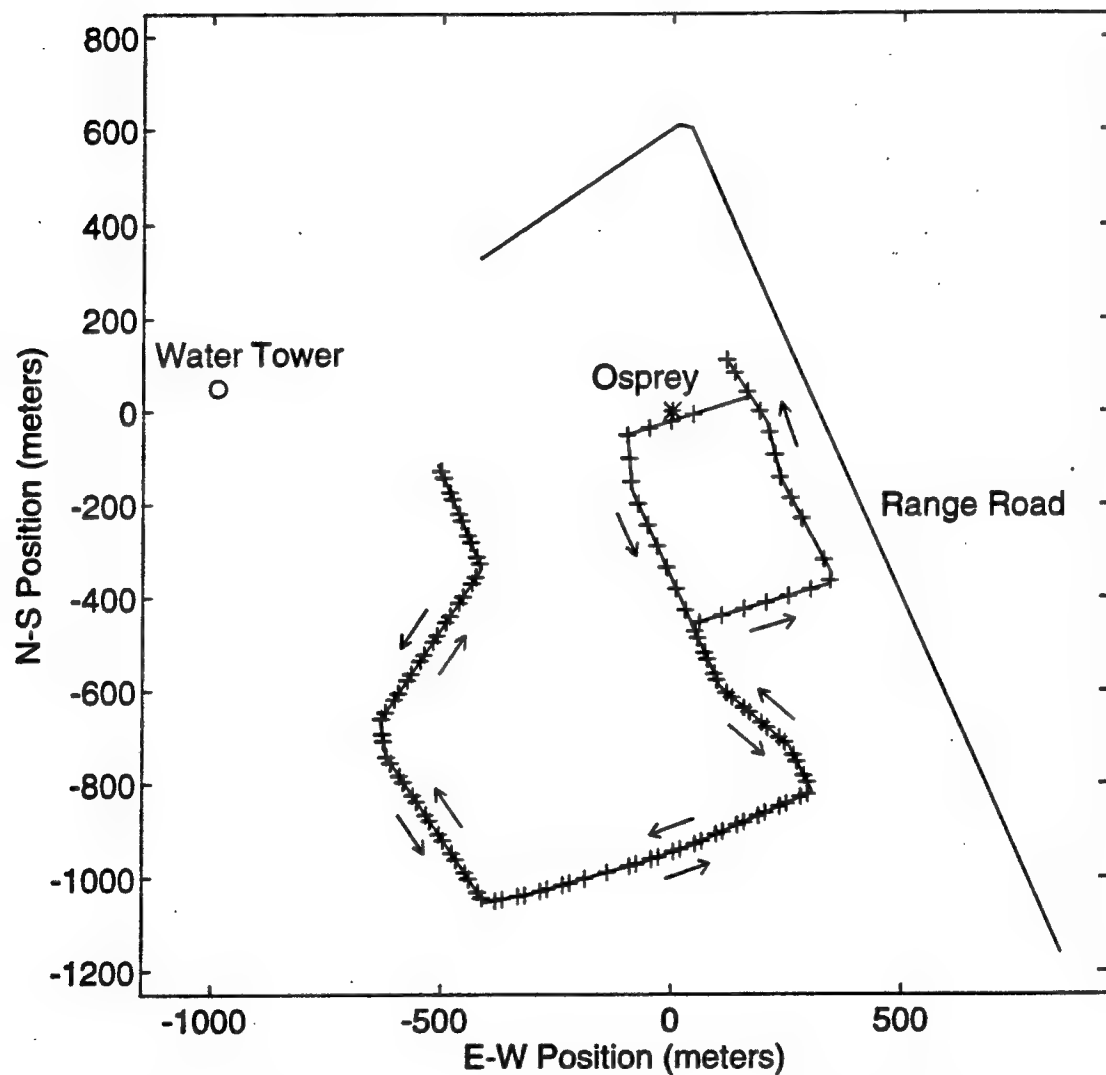


Figure 5: Transmitter locations (marked by +) on March 24, 1993 relative to Osprey system. Arrows show vehicle direction. Start position was $(x_{E-W}, y_{N-S}) = (45, -8)$

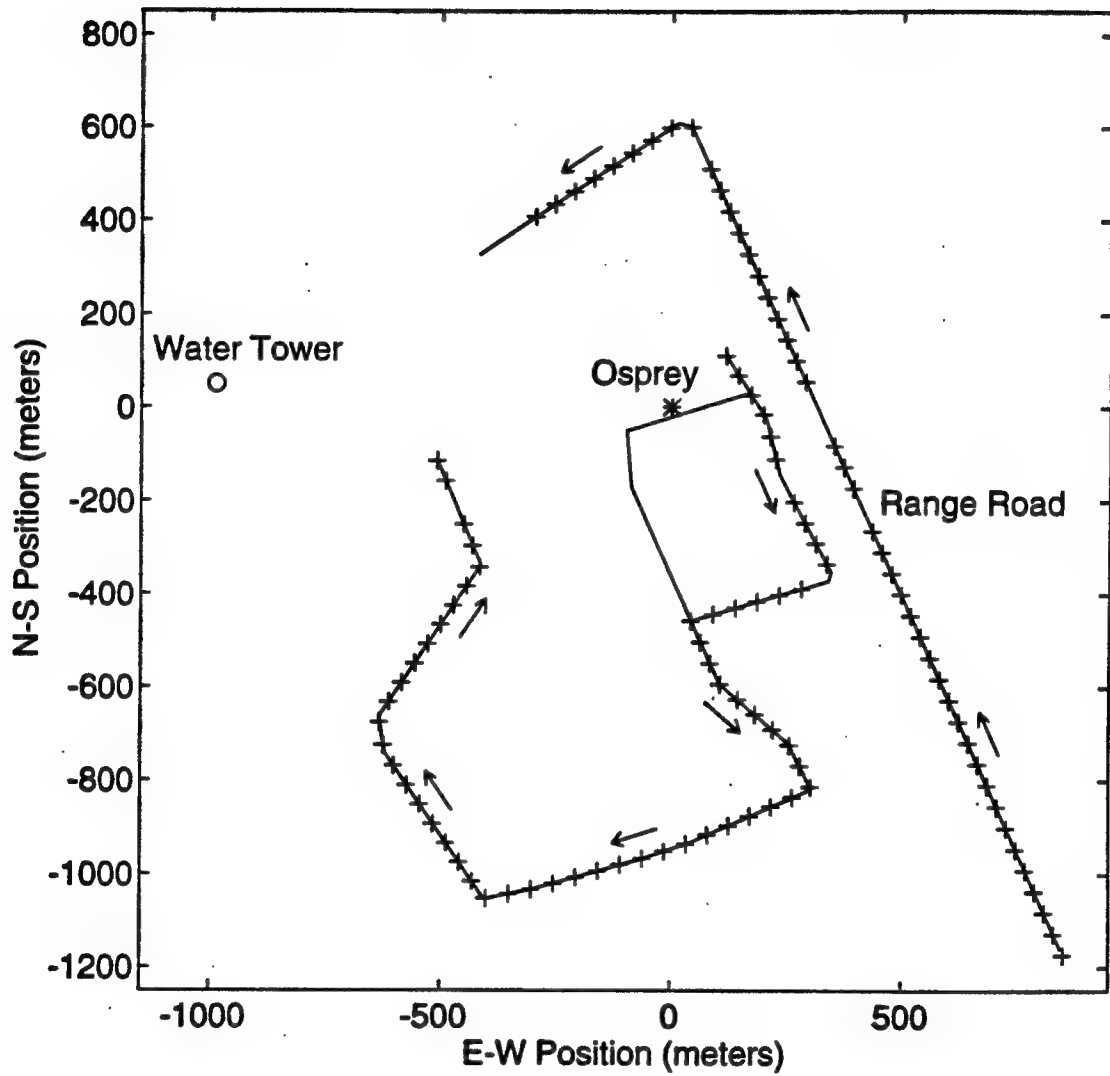


Figure 6: Transmitter locations (marked by +) on March 25, 1993 relative to Osprey system. Arrows show vehicle direction. Start position was $(x_{E-W}, y_{N-S}) = (118, 110)$

3.0 SIGNAL PROCESSING CONSIDERATIONS

3.1 IQ Conversion

An example of the positive frequency spectrum of the raw data is shown in Figure 7. Here a 2048 point FFT (with a Blackman window) was performed on the raw data (2048 samples) collected from antenna 0. The received (down converted) CW signal is clearly evident at 322 Hz along with some interfering signals (likely receiver generated) and the received noise.

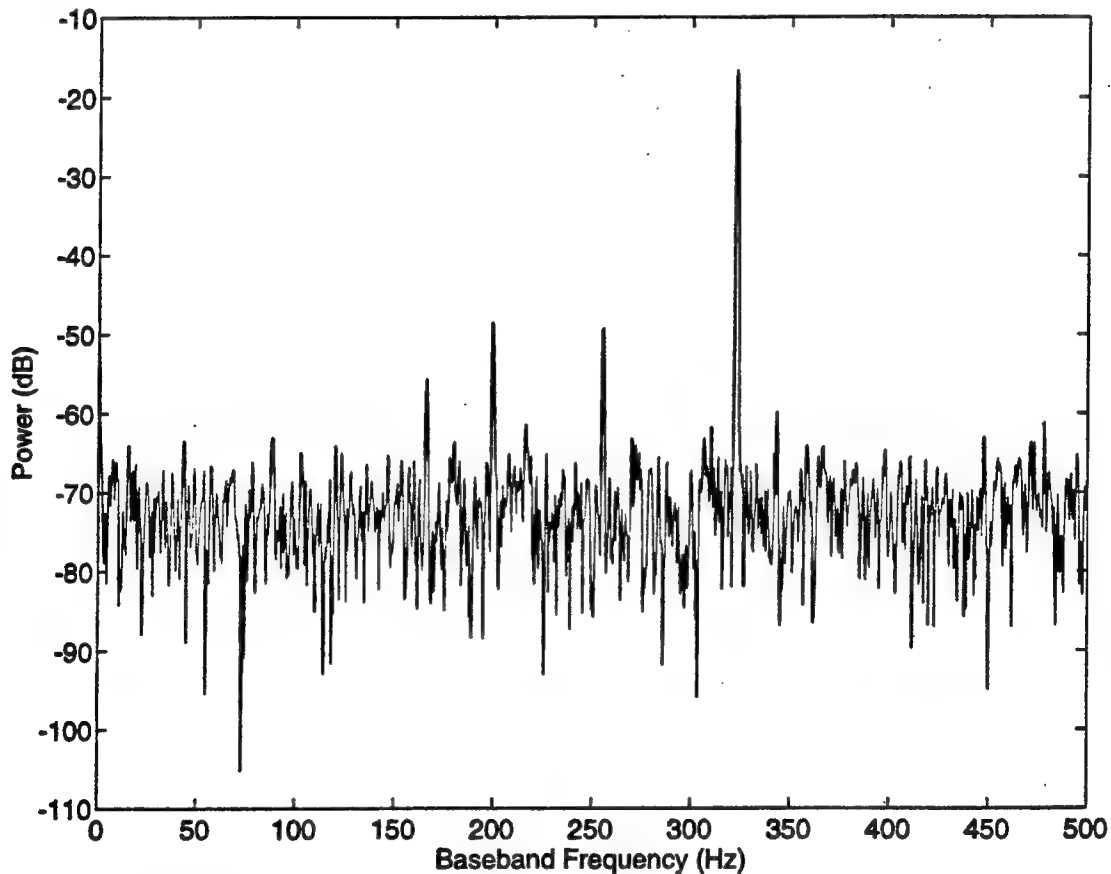


Figure 7: FFT spectrum of raw baseband data from channel 0

For the DF algorithm discussed in this report (Section 3.3), it is more convenient to have the data in complex (I and Q) baseband format. Although many different approaches for accomplishing this are possible, the approach used here is to take advantage of the fact that the signal used was CW. This allows the use of very narrow band filters centered on the signal. Noise and interference outside the filter passband are therefore rejected, significantly improving the signal-to-noise ratio (SNR).

The actual approach is based on the discrete Fourier transform. The definition of the discrete Fourier transform of a data sequence $x_i(k)$ for $k = 0, 1, \dots, K - 1$ is given by,

$$S_i(f_n) = \sum_{k=0}^{K-1} x_i(k) e^{j2\pi f_n k} \quad (1)$$

where i is the antenna number (0 to $N - 1$), f_n is the discrete frequency such that

$$f_n = \frac{nf_s}{K} \quad n = 0, 1, \dots, K - 1 \quad (2)$$

and f_s is the sampling frequency. The transformed data represents the I and Q values of the original data measured at all possible values of f_n . For a CW signal, it is only necessary to determine $S_i(f_o)$ where f_o is the frequency of the CW signal.

One difficulty is that the frequency spectrum can only be calculated at discrete points which are multiples of f_s/K . To improve this situation, zeros padding can be used (i.e. appending zeros to the end of the data) to increase the number of sample points from K to K' . In the limit where $K' \rightarrow \infty$, the frequency becomes a continuous function and $S_i(f)$ can be calculated for any frequency f such that $0 \leq f < f_s$. Note that since $x_i(k) = 0$ for $k > K$, the upper limit of the summation in equation (1) will still be $K - 1$, not $K' - 1$.

In general, the exact frequency of the CW signal will be unknown so that the first step is to perform the Fourier transform without zero padding ($K' = K$). Using the Fast Fourier Transform (FFT) to perform the computations, the approximate frequency f_o is taken as the frequency $f = f_n$ which maximizes the value of $|S_i(f_n)|$. Using this approximate value as a starting point, equation (1) is then used to fine tune the results.

The above approach assumes that the signal-to-interference-plus-noise ratio (SNIR) is high (as in Figure 7) in all of the receive channels, which was true for the experiments described in this report. The choice of which channel i to use is arbitrary, although for consistency, generally $i = 0$ was used. At lower signal levels a more accurate (but computationally more expensive) approach would be to maximize the sum of the power spectra, that is, maximize the function

$$\sum_{i=0}^{N-1} |S_i(f)|^2 \quad (3)$$

where N is the number of sensor channels.

Once the data has been converted to the complex baseband format, a single sample

or snapshot of all N channels is represented by

$$\mathbf{x} = \begin{bmatrix} x_0 \\ x_1 \\ x_2 \\ \vdots \\ x_{N-1} \end{bmatrix} \quad (4)$$

where $x_i = S_i(f_o)$ for $i = 0, 1, \dots, N - 1$ (see also equation (1)). Note that in the IQ processing scheme described above K real data points per channel are collected to generate a single snapshot in IQ form.

For consecutive measurements measured at times starting at $t_0, t_1, t_2, \dots, t_{T-1}$, a data matrix can be formed as,

$$\mathbf{X} = [\mathbf{x}(t_0), \mathbf{x}(t_1), \mathbf{x}(t_2), \dots, \mathbf{x}(t_{T-1})] \quad (5)$$

where $\mathbf{x}(t_n)$ represents a snapshot measured at time t_n , and T is the number of snapshots.

3.2 Channel Equalization

Channel equalization is normally performed in direction finding to ensure that the channel gains and phases are matched. This is often done by disconnecting the receive antennas and replacing the antenna feeds by test signals of identical frequencies, amplitudes, and phases. Adjustable gain and phase devices are then used to adjust the channels until the measured receiver outputs are identical in both gain and phase. This procedure, however, does not account for mismatches introduced by the antennas themselves.

An alternate approach, which has been adopted in this report, is to assume the channel gain and phase mismatches introduced by the equipment were unknown, and then estimate these values based on the measured data collected and some knowledge about the signal environment. Accurate knowledge about the signal environment is critical, otherwise errors are introduced into this approach.

Channel equalization can be performed on the measured data \mathbf{X} using the expression

$$\mathbf{Y} = \mathbf{A}^{-1} \mathbf{X} \quad (6)$$

where \mathbf{Y} is the corresponding $N \times T$ matrix of equalized data, and \mathbf{A} is an $N \times N$ diagonal matrix with complex gain elements $a_0, a_1, a_2, \dots, a_{N-1}$. These complex elements can also be represented in terms of the real valued gain and phase, i.e. for channel k

$(0 \leq k \leq N - 1)$

$$a_k = g_k e^{\theta_k} \quad (7)$$

where g_k is the real-valued gain and θ_k the phase. Since g_k and θ_k are both relative terms, this implies a_k will be ambiguous unless suitable references or constraints are chosen. To remedy this problem the phase is referenced to channel 0 so that

$$\theta_0 = 0 \quad (8)$$

and the gains are normalized so that

$$\sum_{k=0}^{N-1} g_k = N \quad (9)$$

Determination of the complex gain elements a_0, a_1, \dots, a_{N-1} is relatively straight forward if both \mathbf{X} and \mathbf{Y} are known. In reality \mathbf{Y} will not be completely known and therefore must be estimated instead. This estimation requires a complete knowledge of the antenna array and the environment in which it is working. This includes the effects of temporal noise, mutual coupling, and the effects of multipath. Temporal noise can be minimized by performing the measurements at high SNR's (> 30 dB). Mutual coupling effects can be measured or modelled, however, they are ignored in this analysis; the consequences of which are discussed in Section 4.4. Multipath effects are not sufficiently well understood that they can be measured or modelled, hence the estimation of \mathbf{Y} is problematic. However in this analysis special precautions have been taken so that multipath effects can be adequately represented by spatial white noise.

It follows from these assumptions that the equalized array response can be decomposed into a signal and a noise component as

$$\mathbf{Y} = \mathbf{A}^{-1} \mathbf{X} = \mathbf{S} \mathbf{B} + \mathbf{N} \quad (10)$$

where \mathbf{S} is the $N \times T$ signal matrix which is described in more detail below, \mathbf{B} is a diagonal $T \times T$ matrix of complex signal amplitudes, also described below, and \mathbf{N} is the $N \times T$ noise matrix which represents the error due to temporal and spatial noise effects.

The signal matrix \mathbf{S} can be defined in terms of its columns as

$$\mathbf{S} = [\mathbf{s}_0, \mathbf{s}_1, \mathbf{s}_2, \dots, \mathbf{s}_{T-1}] \quad (11)$$

where $\mathbf{s}_0, \mathbf{s}_1, \dots, \mathbf{s}_{T-1}$ are $N \times 1$ signal vectors normalized so that $|\mathbf{s}_k| = 1$ and the first

element s_{k0} is real-valued for $0 \leq k \leq T - 1$. Each signal vector represents the expected response of the antenna array to the signals measured during the corresponding snapshot assuming the array is equalized and there is no noise. If only a single signal is being measured during each snapshot, and the antennas are omnidirectional, then

$$\mathbf{s}_k = \frac{1}{\sqrt{N}} \begin{bmatrix} 1 \\ e^{j\frac{2\pi d}{\lambda} \sin \phi_k} \\ e^{j\frac{4\pi d}{\lambda} \sin \phi_k} \\ \vdots \\ e^{j\frac{2(N-1)\pi d}{\lambda} \sin \phi_k} \end{bmatrix} \quad (12)$$

where d represents the spacing between antennas of the DF array, and $nd \sin \phi_k$ represents the path length difference between sensor n and sensor 0. The assumptions have also been made that the signal is a ground wave with an elevation angle of 0° , and that the shape of the wavefront is planar (i.e. the transmitter is in the farfield of the DF array, and mutual coupling and multipath effects are ignored). In the special case of a single signal, \mathbf{s}_k is also called an *array steering vector*.

The matrix \mathbf{B} is a diagonal matrix with diagonal elements b_0, b_1, \dots, b_{T-1} . The element b_k represents the complex amplitude of the signal vector \mathbf{s}_k in the k^{th} snapshot.

The solution of equation (10) in terms of the complex gains \mathbf{A} involves the simultaneous solution of the complex signal amplitudes in \mathbf{B} , since neither the signal amplitude or phase will be known at the receiving site. The method by which this equation is solved is discussed in Appendix A and is called the *stochastic calibration method* in this report. Since this is a statistical approach (least squares estimation) the greater the number of measurements the better the estimate of the channel gains and phases. This also includes varying the measurements over a wide range of azimuth angles if spatial noise effects are to be minimized.

3.3 The MUSIC DF Algorithm

The Multiple Signal Classification (MUSIC) DF algorithm has been extensively reported in the open literature (for example see references [5]-[7]) and is a popular choice among current superresolution algorithms due to its performance. It is only briefly described here.

Central to the MUSIC algorithm is the $N \times N$ covariance matrix defined by

$$\mathbf{R} = E\{\mathbf{y}\mathbf{y}^H\} \quad (13)$$

where \mathbf{y} represents a single snapshot of equalized data (i.e. a single column of \mathbf{Y}), and the superscript H denotes the conjugate-transpose operation. Generally this quantity is not known exactly but instead estimated from the data using

$$\hat{\mathbf{R}} = \frac{1}{M} \mathbf{Y} \mathbf{Y}^H \quad (14)$$

The covariance matrix is then decomposed in terms of its eigenvectors and eigenvalues as

$$\hat{\mathbf{R}} = \sum_{i=0}^{N-1} \lambda_i \mathbf{v}_i \mathbf{v}_i^H \quad (15)$$

where λ_i represents one of the eigenvalues (which are ordered so that $\lambda_0 \geq \lambda_1 \geq \dots \geq \lambda_5$), and \mathbf{v}_i represents the corresponding eigenvector which are normalized so that $\mathbf{v}_i^H \mathbf{v}_i = 1$.

If it is known that M signals are being received at the tuned frequency then the eigenvectors can be divided into the so-called signal subspace eigenvectors ($\mathbf{v}_0, \dots, \mathbf{v}_{M-1}$) and the noise subspace eigenvectors ($\mathbf{v}_M, \dots, \mathbf{v}_{N-1}$). The MUSIC spectrum is computed using either the noise subspace eigenvectors as

$$S(\phi) = \frac{1}{\sum_{i=M}^{N-1} \mathbf{e}(\phi)^H \mathbf{v}_i \mathbf{v}_i^H \mathbf{e}(\phi)} \quad (16)$$

or the signal subspace eigenvectors as

$$S(\phi) = \frac{1}{1 - \sum_{i=0}^{M-1} \mathbf{e}(\phi)^H \mathbf{v}_i \mathbf{v}_i^H \mathbf{e}(\phi)} \quad (17)$$

Here, $S(\phi)$ is the value of the spectrum at the given azimuth angle, and $\mathbf{e}(\phi)$ is the steering vector defined earlier in Section 3.2 (e.g. see equation (12)). The M largest peaks in the computed spectrum are then taken to correspond to the direction of arrival of the M signals.

4.0 SOURCES OF ERROR

4.1 Transmitter Position

The determination of the bearing errors in the DF estimates is based on comparing the measured bearing with the actual bearing. The actual bearing can be determined from the relative position of the transmitter with respect to the receiver. Defining the position of the Osprey elements in Cartesian coordinates, the position of antenna n for $0 \leq n < N$

is given by

$$(x_n, y_n) = (nd - \frac{1}{2}(N-1)d, 0) \quad (18)$$

Using the center of the antenna array $(x, y) = (0, 0)$ as a reference, the bearing of a transmitter at the location (x_{tx}, y_{tx}) is easily found using

$$\phi = \arctan \left(\frac{x_{tx}}{y_{tx}} \right) \quad (19)$$

where the bearing is measured in a clockwise direction from the y-axis and the range is found using

$$r = \sqrt{x_{tx}^2 + y_{tx}^2} \quad (20)$$

Note that to distinguish position parameters of the form "x" and "y" from data parameters of the form " x " and " y ", only the data parameters are italicized.

In real life, the positions of transmit and receiving antennas will not be known exactly. This introduces errors into the determination of the actual bearing. The amount of error is dependent on the manner in which the position measurements are made.

In the experiments described in this report, the transmitter was moved to successive positions along a roadway. The equipment used to measure the distance between these positions had a minimum resolution of 10 m. This gives a position accuracy of ± 5 m in the direction of the roadway. Position errors due to other sources were assessed to be small enough that they could be ignored. Under these conditions the position error can be considered to be uniformly distributed over the ± 5 m interval with a mean of 0 m. The corresponding RMS position error is $\rho_r = 10/\sqrt{12} = 2.89$ m. Taking the worst case (when the roadway was perpendicular to the signal direction), the RMS bearing error can be calculated using

$$\rho_\phi = \arctan \left(\frac{\rho_r}{r} \right) \quad (21)$$

assuming that $r \gg \rho_r$.

To avoid confusion in the rest of this report, the term "actual bearing" is used when it is assumed the transmitter bearing is known exactly (i.e. theoretical derivations), and the term "map bearing" is used when only an estimate is known (i.e. experimental results). Hence ρ_ϕ represents the RMS map bearing estimation error.

4.2 Noise

The effect of noise (temporal or spatial) is to corrupt the phase and amplitude measurements made at each antenna, which in turn degrades the accuracy of the DF estimation.

An analysis of the optimum estimation error for a linear array against a single signal is given in [5]. Assuming the sensor noise is additive white Gaussian in nature, the mean error in the spatial frequency estimates is zero and the variance given by,

$$\sigma_{\omega}^2 = \frac{6}{snrN(N^2 - 1)} \quad (22)$$

where the spatial frequency, ω_s , is defined here as

$$\omega_s = \frac{2\pi d}{\lambda} \sin \phi \quad (23)$$

and snr is the signal to noise power ratio. In terms of a single equalized snapshot

$$\mathbf{y} = b\mathbf{s} + \mathbf{n} \quad (24)$$

the signal to noise power ratio can be defined as

$$snr = \frac{|b|^2}{|\mathbf{n}|^2} \quad (25)$$

where b is the complex signal amplitude, \mathbf{s} is the signal vector defined by equation (12), and \mathbf{n} is the $N \times 1$ noise vector.

In equation (22), the variance is constant with respect to bearing. To determine the corresponding mean error, $\bar{\phi}_e$, and variance, σ_{ϕ}^2 , of the bearing estimates, the expressions

$$\bar{\phi}_e = \int_{-\infty}^{\infty} f_{\omega}(\tau) \phi_e(\tau) d\tau \quad (26)$$

and

$$\sigma_{\phi}^2 = \int_{-\infty}^{\infty} f_{\omega}(\tau) \phi_e(\tau)^2 d\tau \quad (27)$$

can be used where $f_{\omega}(\tau)$ is the probability distribution function of the spatial frequency errors, and $\phi_e(\tau)$ is the bearing error given by

$$\phi_e(\tau) = \sin^{-1} \left(\frac{\lambda}{2\pi d} (\omega_s + \tau) \right) - \sin^{-1} \left(\frac{\lambda}{2\pi d} \omega_s \right) \quad \text{for } \left| \frac{\lambda}{2\pi d} (\omega_s + \tau) \right| \leq 1 \quad (28)$$

$$\phi_e(\tau) = \sin^{-1} \left(\frac{\omega_s + \tau}{|\omega_s + \tau|} \right) - \sin^{-1} \left(\frac{\lambda}{2\pi d} \omega_s \right) \quad \text{for } \left| \frac{\lambda}{2\pi d} (\omega_s + \tau) \right| > 1 \quad (29)$$

Equation (29) is a result of the fact that the bearings for a linear array are real-valued and restricted to the range $\pm 90^\circ$. For example, given a transmitter bearing of 89° and a low

value of snr , the maximum positive bearing error cannot exceed 1° while the maximum negative bearing error could be as much as -179° . The bearing errors in this case are very asymmetric with respect to zero error.

Assuming $snr > 1$, then $f_\omega(\tau)$ can be reasonably approximated as having the same distribution as the input noise, namely, a zero-mean white Gaussian distribution. Therefore,

$$f_\omega(\tau) = \frac{1}{\sqrt{2\pi}\sigma_\omega} e^{-\frac{\tau^2}{2\sigma_\omega^2}} \quad (30)$$

Since this leads to integrations (equations (26) and (27)) which are difficult to perform algebraically, they were performed numerically and the results shown in Figure 8. In this figure the absolute value of the mean errors ($|\bar{\phi}_e|$) and the standard deviation (σ_ϕ) of the bearing errors measured (theoretically) using the Osprey array at $f = 62.5$ MHz are plotted as a function of signal bearing for several different signal to noise ratios. Noise was assumed to be the only source of error.

The theoretical RMS bearing error is given by

$$\phi_{eRMS} = \sqrt{\bar{\phi}_e^2 + \sigma_\phi^2} \quad (31)$$

From the results shown in Figure 8, the mean error is significantly smaller than the standard deviation for the same bearing and SNR. therefore a reasonable approximation for the RMS bearing error is given by

$$\phi_{eRMS} = \sigma_\phi \quad (32)$$

From these results it is also clear that the best accuracy (lowest RMS error) is achieved for the broadside direction (0° azimuth) of the array and that accuracy significantly degrades towards the endfire directions ($\pm 90^\circ$ azimuth). The "corner effect" that occurs near endfire (e.g. at approx 75° on the $SNR = 0$ dB curve) is due to the asymmetry effect described earlier.

For conditions where the signal to noise ratio is greater than 0 dB ($snr > 1$), the accuracy of the Osprey array can be reasonably approximated by simpler expressions. Away from the endfire directions, a reasonable approximation of the accuracy is given by,

$$\sigma_\phi = \frac{\sigma_\omega \lambda}{2\pi d |\cos \phi|} \quad (33)$$

In the endfire position, the term $\cos \phi$ goes to 0 and the above expression for accuracy no longer holds. Instead, it has been found empirically that accuracy can be approximated

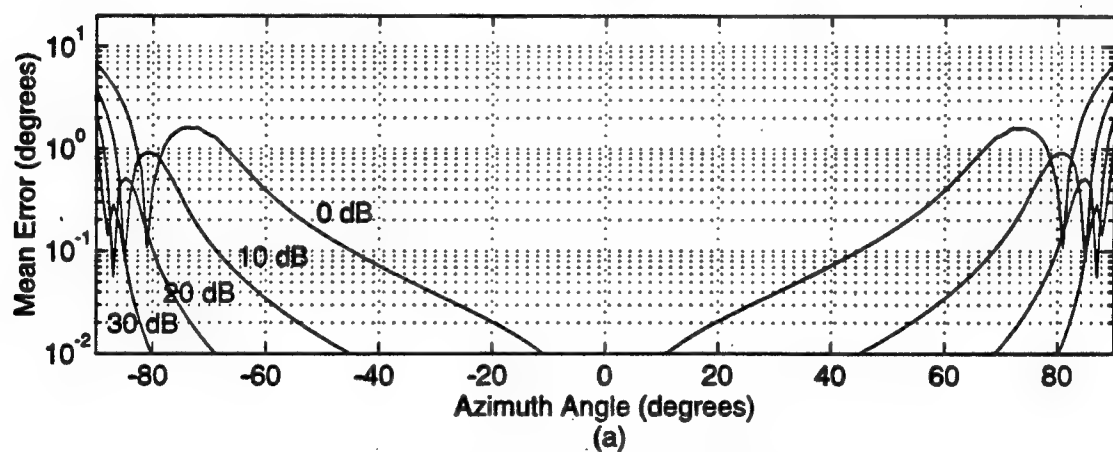
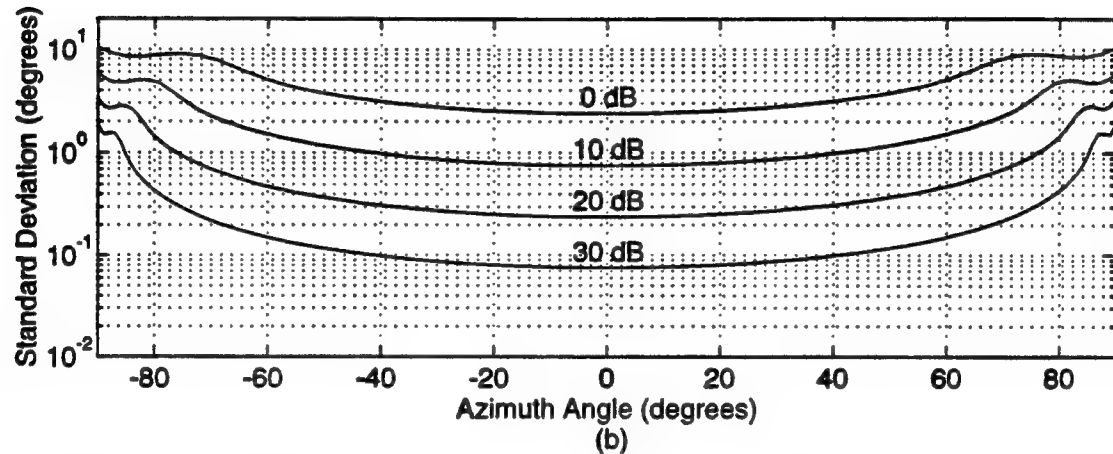


Figure 8: Theoretical absolute mean bearing error (a) and bearing variance (b) of the Osprey System as a function of signal bearing and SNR.

by

$$\sigma_\phi = \sqrt{\frac{\sigma_\omega \lambda}{\pi^2 d}} \quad (34)$$

It is interesting to note that in the endfire case, the accuracy is proportional to $snr^{-\frac{1}{4}}$ compared to $snr^{-\frac{1}{2}}$ for the broadside case.

Although the analysis of noise effects has been carried out using white Gaussian noise assumptions, it does provide a good approximation of the sensitivity of the array to errors as a function of signal direction. That is, the exact values of the variance may change slightly depending on the error mechanism involved, but the shapes and trends (especially towards endfire) exhibited by the curves in Figure 8 would be expected to stay the same.

Given that the endfire effects are due solely to the $\sin^{-1}(\cdot)$ transformation between spatial frequency and azimuth bearing, and potentially could mask other underlying error mechanisms (besides noise), it is useful to normalize the error results accordingly. One way is to compute the spatial frequency errors, rather than the actual bearing errors, and then convert these to bearing errors as if the signal bearing had originally been zero degrees. This is equivalent to using

$$\phi_e(\tau) = \sin^{-1} \left(\frac{\lambda}{2\pi d} \tau \right) \quad (35)$$

instead of equation (29) where τ is the spatial frequency error. In the case where only the true and estimated bearings are known, the corresponding spatial frequencies can be computed using equation (23). In terms of accuracy, the effect of this normalization is to artificially rotate the array so that the array baseline is always perpendicular to the signal source. For any given signal to noise ratio, the accuracy is then predicted by the values for $\phi = 0^\circ$ in Figure 8. For obvious reasons this normalization process is called *broadside normalization*.

4.3 Wind Effects

The effect of the wind on the Osprey antenna array is to perturb the antennas from their known positions. Ignoring all other error mechanisms the perturbed output at antenna n will be,

$$y_n = s e^{-j \frac{2\pi}{\lambda} (d \sin \phi + \delta_{xn} \sin \phi + \delta_{yn} \cos \phi)} \quad (36)$$

where δ_{xn} and δ_{yn} are the displacements of the antenna from its ideal position in the x and y directions, respectively. In reference [6], an expression of the effects of y direction position errors (i.e. $\delta_{xn} = 0$) on bearing error variance is developed. In this analysis it is

assumed that δ_{yn} has a Gaussian distribution and $|\delta_{yn}| \ll d$. Using this expression and converting it to the equivalent spatial frequency error variance (this is done so that the contribution in the x direction can be more readily included), the result is given by

$$\sigma_\omega^2 = \frac{12}{N(N^2 - 1)} \left(\frac{2\pi d}{\lambda} \sigma_y \cos \phi \right)^2 \quad (37)$$

where σ_y^2 is the position error variance in the y direction and is assumed to be the same for all antennas. Noting the similarity between the effects of the errors $\delta_{xn} \sin \phi$ and $\delta_{yn} \cos \phi$ in equation (36), then one can easily modify equation (37) to include the effects of $0 < |\delta_{xn}| \ll d$. Making the same assumptions for δ_{xn} as for δ_{yn} and also assuming δ_{xn} and δ_{yn} to be uncorrelated, the modified expression becomes

$$\sigma_\omega^2 = \frac{12}{N(N^2 - 1)} \left(\frac{2\pi d}{\lambda} \right)^2 (\sigma_x^2 \sin^2 \phi + \sigma_y^2 \cos^2 \phi) \quad (38)$$

where σ_x^2 is the position error variance in the x direction. In the special case where $\sigma_x = \sigma_y = \sigma_{xy}$, this simplifies to,

$$\sigma_\omega^2 = \frac{12}{N(N^2 - 1)} \left(\frac{2\pi d \sigma_{xy}}{\lambda} \right)^2 \quad (39)$$

The conversion of the spatial frequency error variance to bearing error variance proceeds in the same manner as the noise case (i.e. using equations (27)-(34)).

Some comments about the above expression are in order here. The antennas used for the Osprey array have a very small wind cross section and are sufficiently rigid that for all but the most extreme weather conditions the values of δ_{xn} and δ_{yn} are small compared to the antenna spacing.

The antennas are also identical which means that the position error variances for each antenna will be identical. This also means that the antennas would be expected to bend in approximately the same direction when the wind blows. Consequently the position errors will be correlated from sensor to sensor. Since small position translations of the array have no effect on the DF results, then equations (38) and (39) can be regarded as upper bounds on the error. Alternately, δ_{xn} and δ_{yn} (and correspondingly σ_x and σ_y) can be interpreted as the position errors which result after the effective position translation of the whole array due to the wind has been taken into account (i.e. subtracted out).

Over short periods of time, the wind direction will be constant with the result that the perturbations δ_{xn} and δ_{yn} will be highly correlated. Therefore equations (38) and (39)

are assumed to apply for time periods long enough that δ_{xn} and δ_{yn} decorrelate.

The preceding analysis does not take into account the change in the mutual coupling or polarization response of the antennas when bending occurs. These effects have been ignored for the following reasons. Mutual coupling is caused by reradiation of the incident electric field by the antennas (and support structure) themselves. Changing antenna position affects the amount of reradiated signal power received at each antenna. Since this is a secondary effect (i.e. the reradiated power received by one antenna from another antenna will be significantly less than from the power received from the transmitter — see the following section on mutual coupling), the bearing errors introduced by this effect will be correspondingly less than those discussed in the preceding paragraphs. In the case of the polarization response, the amplitude gain of a dipole antenna for vertically/horizontally polarized signals is a function of the cosine/sine of the bending angle [7]. For the small bending angles observed in practise ($< 1^\circ$), and even assuming the incident vertical and horizontal electric fields are completely different, the bearing errors introduced are negligible.

4.4 Mutual Coupling

Mutual coupling effects arise from the fact that each antenna modifies the electric field locally by retransmitting a portion of the received signal. The amount of coupling between antennas is therefore a function of the ratio of the received signal power to the retransmitted signal and the distances between antennas.

In the case of the Osprey array, there are several observations which simplify the analysis. The first is the small electrical radii of the dipole elements ($< 0.01\lambda$) which means dipole current will only be in the vertical direction. The second is that the directional or beam pattern of a vertical dipole is omnidirectional in azimuth. The third is that each element lies in the same vertical plane. All these features ensure that an expression describing mutual coupling effects will be dependent only on the distance between antennas and independent of signal bearing in both azimuth and elevation.

Based on these observations, the analysis of mutual coupling can be treated in terms of an equivalent electric circuit. For example, the equivalent circuit for antenna 0 in a two antenna system is shown in Figure 9 where V_0 is the voltage due the signal source (transmitter), V_{01} is the voltage induced in antenna 0 via reradiation from antenna 1, Z_{r0} is the self impedance of the antenna, Z_{l0} is the load impedance, and V_0 is the voltage across the two impedances. The voltages in this circuit have the relationship

$$V_0 = V_0 + V_{01} \quad (40)$$

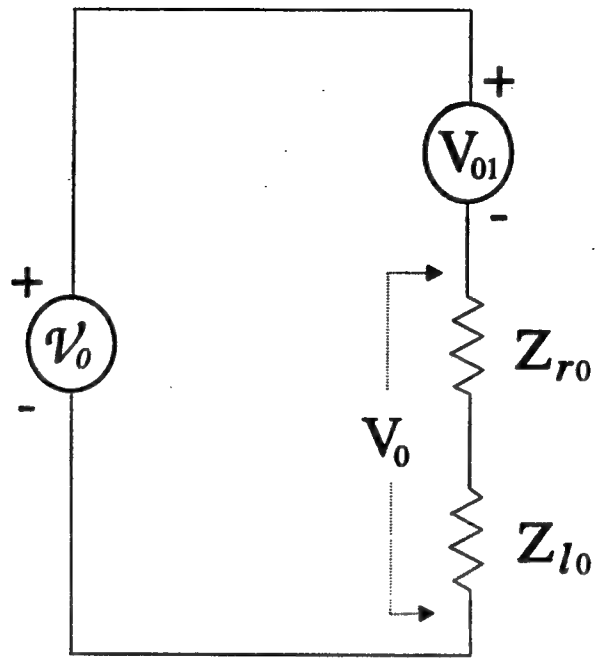


Figure 9: Equivalent electrical circuit for antenna 0.

The voltage induced in antenna 0 by antenna 1 can be related to the current in antenna 1 by the expression

$$V_{01} = I_1 Z_{01} \quad (41)$$

where Z_{01} is defined as the mutual impedance between antennas 0 and 1. Adopting a similar equivalent circuit definition for antenna 1 as given for antenna 0 (shown in Figure 9), then the current in antenna 1 can be determined using

$$I_1 = \frac{V_1}{Z_{r1} + Z_{l1}} \quad (42)$$

Plugging this last result into equation (41) and then back into equation (40) gives

$$V_0 = V_0 + V_1 \left(\frac{Z_{01}}{Z_{r1} + Z_{l1}} \right) \quad (43)$$

Similarly for antenna 1,

$$V_1 = V_1 + V_0 \left(\frac{Z_{10}}{Z_{r0} + Z_{l0}} \right) \quad (44)$$

These results are easily generalized to an N element array to get

$$\mathcal{V}_k = \sum_{i=0}^{N-1} V_i \left(\frac{Z_{ki}}{Z_{r_i} + Z_{l_i}} \right) \quad \text{for } k = 0, 1, 2, \dots, N-1 \quad (45)$$

where $Z_{ii} = Z_{r_i} + Z_{l_i}$. Since \mathcal{V}_k is the voltage that would be measured by an ideal sensor (i.e. the voltage due to the transmitter only), it is the voltage of interest for DF purposes. In reality the only sensor voltages available will be the load voltages V_{l_k} ($k = 0, 1, \dots, N-1$). Since Z_{l_k} and Z_{r_k} form a voltage divider, V_{l_k} can be related to V_k using

$$V_k = V_{l_k} \left(\frac{Z_{r_k} + Z_{l_k}}{Z_{l_k}} \right) \quad (46)$$

Equation (45) then becomes

$$\mathcal{V}_k = \sum_{i=0}^{N-1} V_i \left(\frac{Z_{ki}}{Z_{l_i}} \right) \quad \text{for } k = 0, 1, 2, \dots, N-1 \quad (47)$$

The system of equations represented by equation (47) can also be written in matrix form as

$$\mathbf{z} = \mathbf{Qy} \quad (48)$$

where \mathbf{z} represents the ideal antenna voltage with $z_k = \mathcal{V}_k$, \mathbf{y} represents the measured antenna output voltage (after equalization) with $y_k = V_{l_k}$, and \mathbf{Q} is the $N \times N$ impedance ratio matrix with elements

$$q_{ki} = \frac{Z_{ki}}{Z_{l_i}} \quad (49)$$

When $i = k$ the above expression can also be written as

$$q_{kk} = \frac{Z_{r_k} + Z_{l_k}}{Z_{l_k}} \quad (50)$$

For dipole antennas, the mutual impedance can be represented as

$$Z_{ki} = R_{ki} + jX_{ki} \quad (51)$$

where R_{ki} is the resistive element and X_{ki} is the reactive element. An analytical expression for these elements is given by [7], [8]

$$R_{ki} = \frac{30}{\sin^2(\kappa L/2)} \left(2(2 + \cos(\kappa L)) \text{Ci}(\kappa r_{ki}) - \right.$$

$$\begin{aligned}
& -4 \cos^2\left(\frac{\kappa L}{2}\right) \left[\text{Ci}\left(\frac{\kappa}{2}(\sqrt{4r_{ki}^2 + L^2} - L)\right) + \text{Ci}\left(\frac{\kappa}{2}(\sqrt{4r_{ki}^2 + L^2} + L)\right) \right] \\
& + \cos(\kappa L) \left[\text{Ci}\left(\kappa(\sqrt{r_{ki}^2 + L^2} + L)\right) + \text{Ci}\left(\kappa(\sqrt{r_{ki}^2 + L^2} - L)\right) \right] \\
& + \sin(\kappa L) \left[\text{Si}\left(\kappa(\sqrt{r_{ki}^2 + L^2} + L)\right) - \text{Si}\left(\kappa(\sqrt{r_{ki}^2 + L^2} - L)\right) \right. \\
& \left. - 2\text{Si}\left(\frac{\kappa}{2}(\sqrt{4r_{ki}^2 + L^2} + L)\right) + 2\text{Si}\left(\frac{\kappa}{2}(\sqrt{4r_{ki}^2 + L^2} - L)\right) \right] \quad (52)
\end{aligned}$$

$$\begin{aligned}
X_{ki} = & \frac{-30}{\sin^2(\kappa L/2)} \left(2(2 + \cos(\kappa L))\text{Si}(\kappa r_{ki}) - \right. \\
& - 4 \cos^2\left(\frac{\kappa L}{2}\right) \left[\text{Si}\left(\frac{\kappa}{2}(\sqrt{4r_{ki}^2 + L^2} - L)\right) + \text{Si}\left(\frac{\kappa}{2}(\sqrt{4r_{ki}^2 + L^2} + L)\right) \right] \\
& + \cos(\kappa L) \left[\text{Si}\left(\kappa(\sqrt{r_{ki}^2 + L^2} + L)\right) + \text{Si}\left(\kappa(\sqrt{r_{ki}^2 + L^2} - L)\right) \right] \\
& - \sin(\kappa L) \left[\text{Ci}\left(\kappa(\sqrt{r_{ki}^2 + L^2} + L)\right) - \text{Ci}\left(\kappa(\sqrt{r_{ki}^2 + L^2} - L)\right) \right. \\
& \left. - 2\text{Ci}\left(\frac{\kappa}{2}(\sqrt{4r_{ki}^2 + L^2} + L)\right) + 2\text{Ci}\left(\frac{\kappa}{2}(\sqrt{4r_{ki}^2 + L^2} - L)\right) \right] \quad (53)
\end{aligned}$$

where $r_{ki} = |k - i|d$ is the distance between antennas k and i , $\kappa = 2\pi/\lambda$, and $\text{Ci}(\cdot)$ and $\text{Si}(\cdot)$ are the cosine and sine integrals defined as

$$\text{Ci}(x) = \int_{\infty}^x \frac{\cos v}{v} dv = 0.5772 + \ln x - \frac{x^2}{2!2} + \frac{x^4}{4!4} - \frac{x^6}{6!6} + \dots \quad (54)$$

and

$$\text{Si}(x) = \int_0^x \frac{\sin v}{v} dv = x - \frac{x^3}{3!3} + \frac{x^5}{5!5} - \frac{x^7}{7!7} + \dots \quad (55)$$

The impedance Z_{kk} consists of the antenna self impedance Z_{r_k} and the load impedance Z_{l_k} . For maximum power transfer (i.e. a matched system), the load impedance $Z_{l_k} = Z_{r_k}^*$ which results in $Z_{kk} = 2\text{real}\{Z_{r_k}\}$. The self impedance Z_{r_k} can be computed using equations (51)-(55) where r_{ki} is equated to the radius of the dipole elements (0.3 cm for the dipoles of the Osprey array).

Equations (51)-(55) predict identical mutual impedance for any pair elements provided the spacing is the same. In reality, this will not be exactly true due to electrical and physical differences between the antennas, and mismatches introduced by cables, cable couplings, etc. However these equations should be sufficiently accurate to characterize the resulting errors introduced into DF estimation and approximately quantify these errors. In this light, Figures 10 and 11 show the performance of the Osprey with mutual coupling effects included and assuming the antennas are perfectly matched. The frequency chosen for simulation was 62.5 MHz.

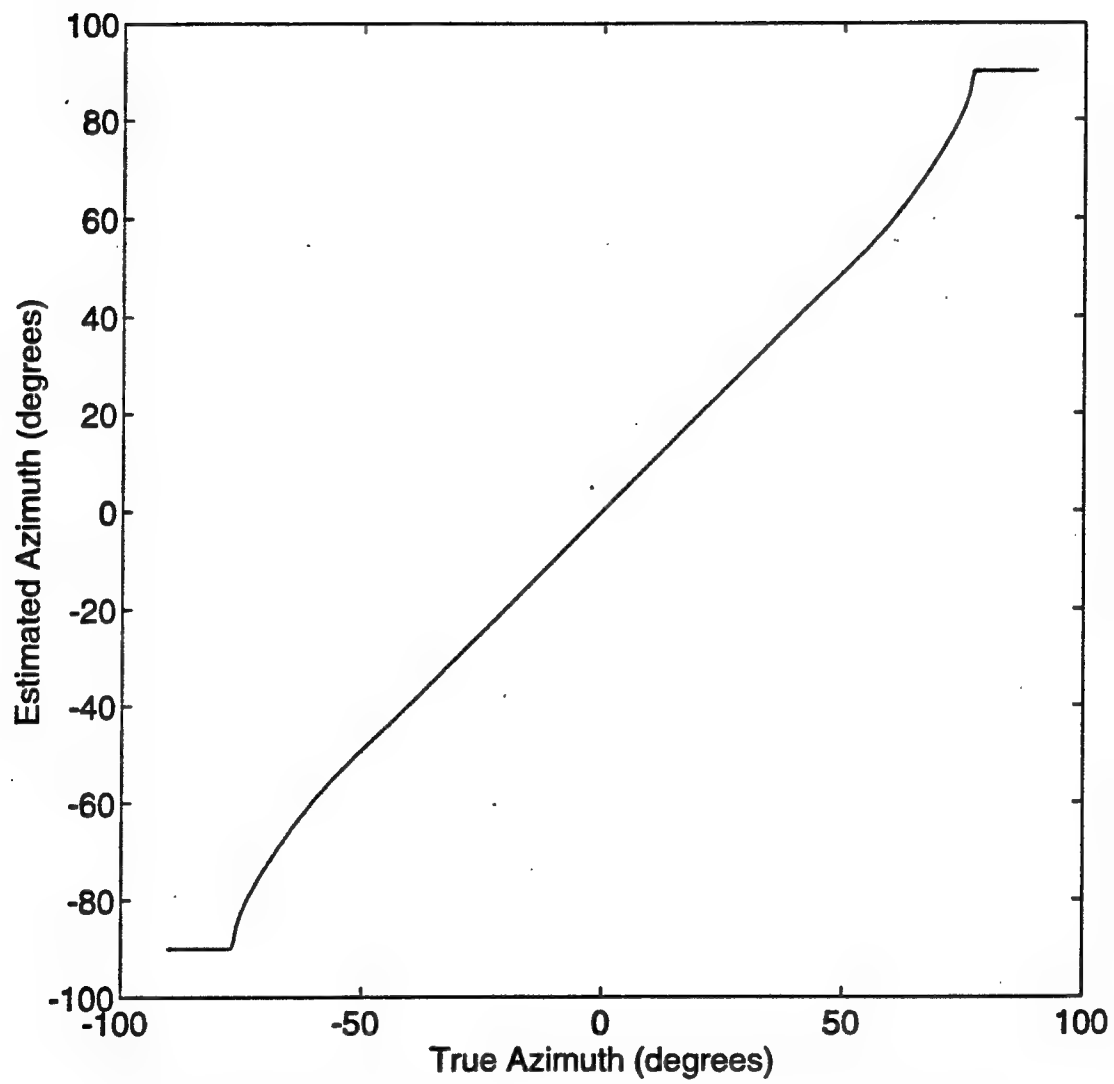


Figure 10: Estimated bearing versus true bearings with mutual coupling.

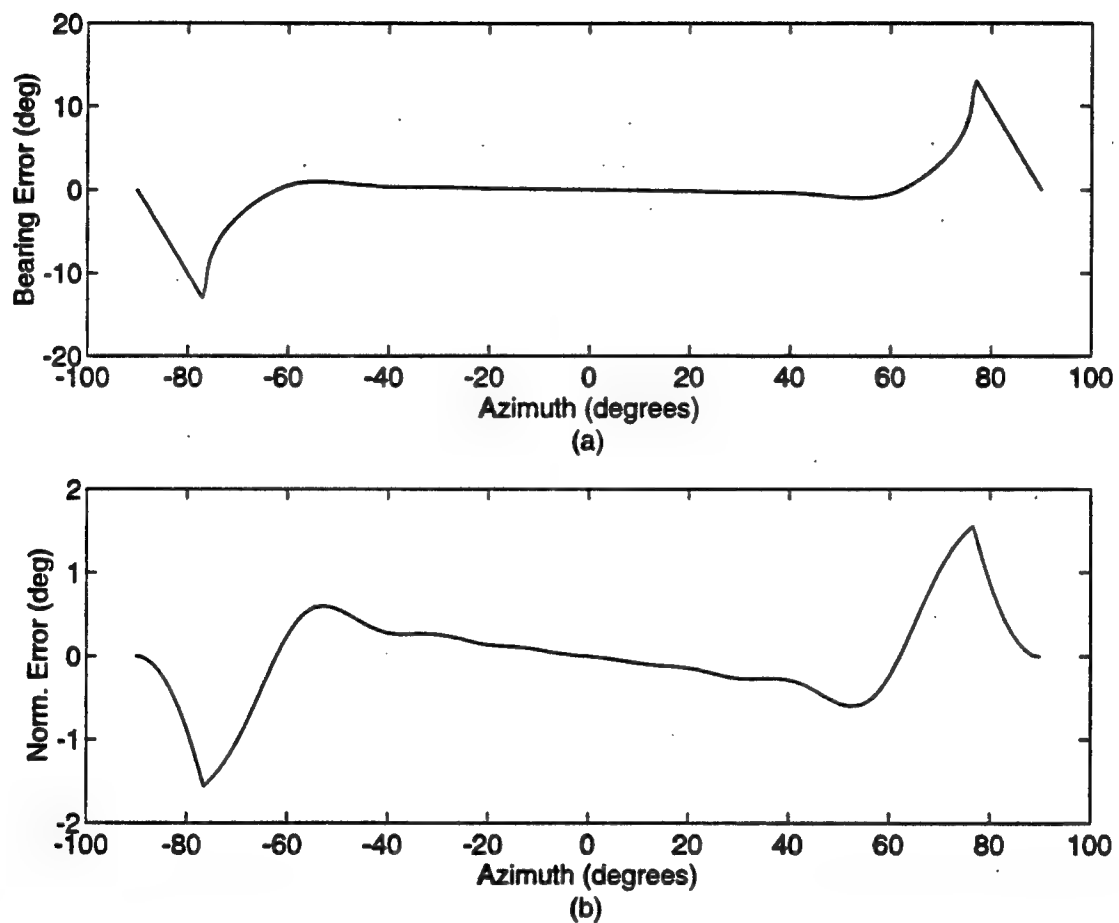


Figure 11: Corresponding bearing errors: (a) actual (b) after broadside normalization.

Figure 10 plots the estimated bearings versus the true bearings. The most significant errors occur towards the end fire direction with the estimated bearings locking onto $\pm 90^\circ$ once the actual bearing reaches $\pm 77^\circ$. The lock on effect is a result of the mutual coupling which increases the magnitude of the measured spatial frequency, compared to the true frequency, for signal directions near endfire. This causes a corresponding increase in the measured bearing magnitude so that if the true bearing is increasing in magnitude the measured bearing will reach $\pm 90^\circ$ before the true bearing does. Since a linear array can only measure bearings in the range $+90^\circ$ to -90° , increasing the magnitude of the transmitter bearing beyond this point has no effect on the measured bearing, i.e. the measured bearing will remain locked on $\pm 90^\circ$.

Figure 11a shows the corresponding bearing error. Figure 11b shows the errors after broadside normalization (defined previously by equation 35)) and illustrates that not all the increased endfire error is attributable to the conversion from spatial frequency to bearing. The RMS errors for Figure 11 were 3.5° for (a) and 0.5° for (b).

A final, but important observation about mutual coupling is that the resultant error response does not fluctuate rapidly with azimuth and that it is invariant with time (ignoring equipment aging and minor wind effects) — important distinguishing characteristics which are useful when other error effects are included in the analysis.

4.5 Multipath

VHF multipath and its effects on communications systems have been extensively researched and reported in the open literature (e.g. *IEEE Transactions on Antennas and Propagation*). To the author's knowledge, very little research has been done on VHF multipath and its effects on direction finding antenna arrays. DF research differs from communications research in the fact that not only is received signal power an important consideration, but so is the shape of the incident signal waveform.

Some idea of the complexity of the DF problem can be realized by considering the ground conditions over which the radio signal is transmitted. In the rural country side around DREO, ground conditions are very non-uniform, i.e., varying ground conductivities, numerous random obstacles such as rocks, hills, trees, forests, power lines, fences, buildings, etc., and varying size and conductivities of these obstacles. This results in the generation of a multitude of secondary signals through diffraction, reflection, reradiation, refraction and scattering effects, which adversely affects DF accuracy.

There have been efforts made at DREO to model these effects with the aim of better understanding the consequences for direction finding. Reporting on this research in detail is beyond the scope of this report, however, it is worth describing some of the more general

results which have relevance to the experimental measurements described in this report.

In order to keep the following analysis relatively simple, a number of assumptions have been made. These assumptions are:

1. Ray theory is applicable
2. All antennas are isotropic
3. Farfield conditions are assumed
4. Antenna heights are insignificant compared to the transmitter receiver range
5. The transmitter is the phase reference

The first assumption allows path losses and corresponding phase delays to be calculated in a relatively straight forward manner. However, it does not provide any indication of the scattering that occurs when the signal wavefront encounters an obstacle. The second, third, and fourth assumptions simplify the mathematics and only degrade the results when the effect of multipath sources within a few wavelengths of either the transmitting or receiving antennas are considered. The last assumption provides a common reference for the phase calculations.

In the following three sections, the multipath model is developed beginning with freespace propagation, followed by the inclusion of ground reflections, and ending with the development of idealized multipath sources and their effect on propagation.

4.5.1 Freespace model

Proceeding from the assumptions just described, the received signal can be determined for a given transmitted signal based on power considerations. For an isotropic transmitter source in freespace, the radio wave expands in a spherical wave with the transmitter source at the center. The power extracted by a receiving antenna at a distance r from a transmitting antenna will be in direct proportion to the area of the spherical wave μ intercepted by the antenna compared to the total area $4\pi r^2$ of the spherical wave — see Figure 12. If the collecting area of the antenna is circular, the received power will be given by,

$$P_{recv} = \frac{P_{tx}}{2} \left(1 - \frac{1}{\sqrt{1 + \frac{\mu}{4\pi r^2}}} \right) \quad (56)$$

where P_{recv} is the received signal power, P_{tx} is the power radiated by the transmitter, and μ is the effective collecting area of the receiving antenna. For an isotropic receiving

antenna $\mu = \frac{\lambda^2}{4\pi}$ [7], and equation (56) becomes,

$$P_{recv} = \frac{P_{tx}}{2} \left(1 - \frac{1}{\sqrt{1 + (\frac{\lambda}{2\pi r})^2}} \right) \quad (57)$$

For $r \gg \lambda$ this simplifies to

$$P_{recv} = P_{tx} \left(\frac{\lambda}{4\pi r} \right)^2 \quad (58)$$

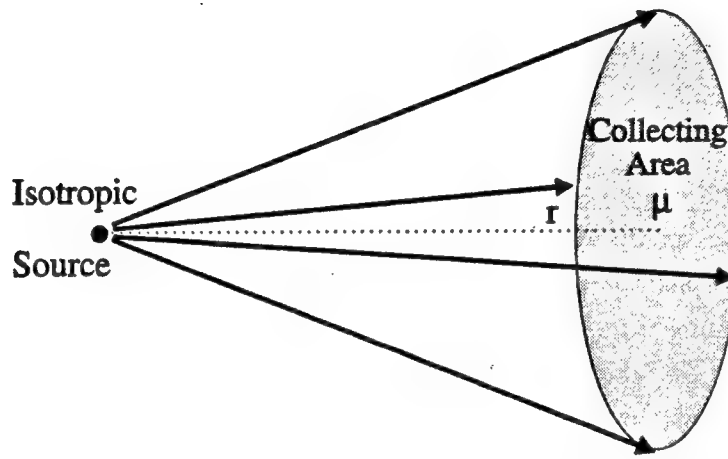


Figure 12: Effective collecting area of an isotropic antenna.

It is often useful to express the path loss as a relative quantity. Accordingly, the freespace path loss l_{free} , is defined here as the ratio of the received signal power to the transmitted power, or

$$l_{free} = \left(\frac{\lambda}{4\pi r} \right)^2 \quad (59)$$

The complex amplitude s_{recv} of the received signal can also be related to that of the amplitude of the transmitted signal s_{tx} (which is real valued since the transmitter is the phase reference) using the fact that $|s| \propto P^{\frac{1}{2}}$ (where s and P represent signal amplitude and power respectively) and the phase delay is a function of the path length r . This leads to the result

$$s_{recv} = s_{tx} \left(\frac{\lambda}{4\pi r} \right) e^{-j\frac{2\pi r}{\lambda}} \quad (60)$$

4.5.2 Plane Earth Model

For signal paths over land, the ground plays a prominent role in propagation loss. Beginning with the plane earth model, as shown in Figure 13, the received signal is the sum of the direct signal and the ground reflected signal. The direct signal can be calculated using the freespace equations to give

$$s_{dir} = s_{tx} \left(\frac{\lambda}{4\pi r_0} \right) e^{-j\frac{2\pi}{\lambda} r_0} \quad (61)$$

where s_{tx} is the amplitude of the signal measured at the transmitter. The ground reflected signal can be calculated in a similar fashion to get

$$s_{ref} = s_{tx} R_v \left(\frac{\lambda}{4\pi(r_1 + r_2)} \right) e^{-j\frac{2\pi}{\lambda}(r_1 + r_2)} \quad (62)$$

where R_v is the ground reflection coefficient. In terms of the direct signal s_{dir} this becomes

$$s_{ref} = s_{dir} R_v \left(\frac{r_0}{r_1 + r_2} \right) e^{-j\frac{2\pi}{\lambda}(r_1 + r_2 - r_0)} \quad (63)$$

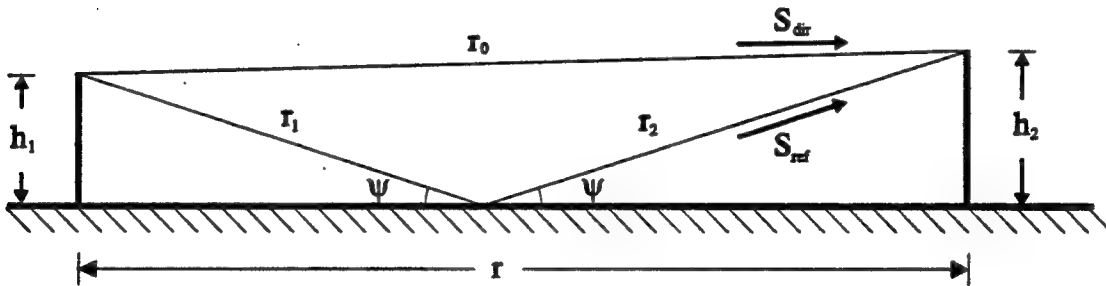


Figure 13: Plane Earth propagation model.

Assuming $r_1, r_2 \gg h_1, h_2$ then the first bracketed term in equation (63) can be approximated as

$$\frac{r_0}{r_1 + r_2} = 1 \quad (64)$$

and further assuming $r\lambda \gg h_1 h_2$ then the second bracketed term (which is part of the exponential term) in equation (63) can be approximated by

$$r_1 + r_2 - r_0 = \frac{2h_1 h_2}{r} \quad (65)$$

are valid, and the expression for the reflected signal s_{ref} can be simplified to

$$s_{ref} = s_{dir} R_v e^{-j \frac{4\pi h_1 h_2}{r\lambda}} \quad (66)$$

$$\approx s_{dir} R_v \left(1 - j \frac{4\pi h_1 h_2}{r\lambda} \right) \quad (67)$$

The combined signal $s_{rcvr} = s_{dir} + s_{ref}$ is given by,

$$s_{rcvr} = s_{dir} \left(1 + R_v - j R_v \frac{4\pi h_1 h_2}{r\lambda} \right) \quad (68)$$

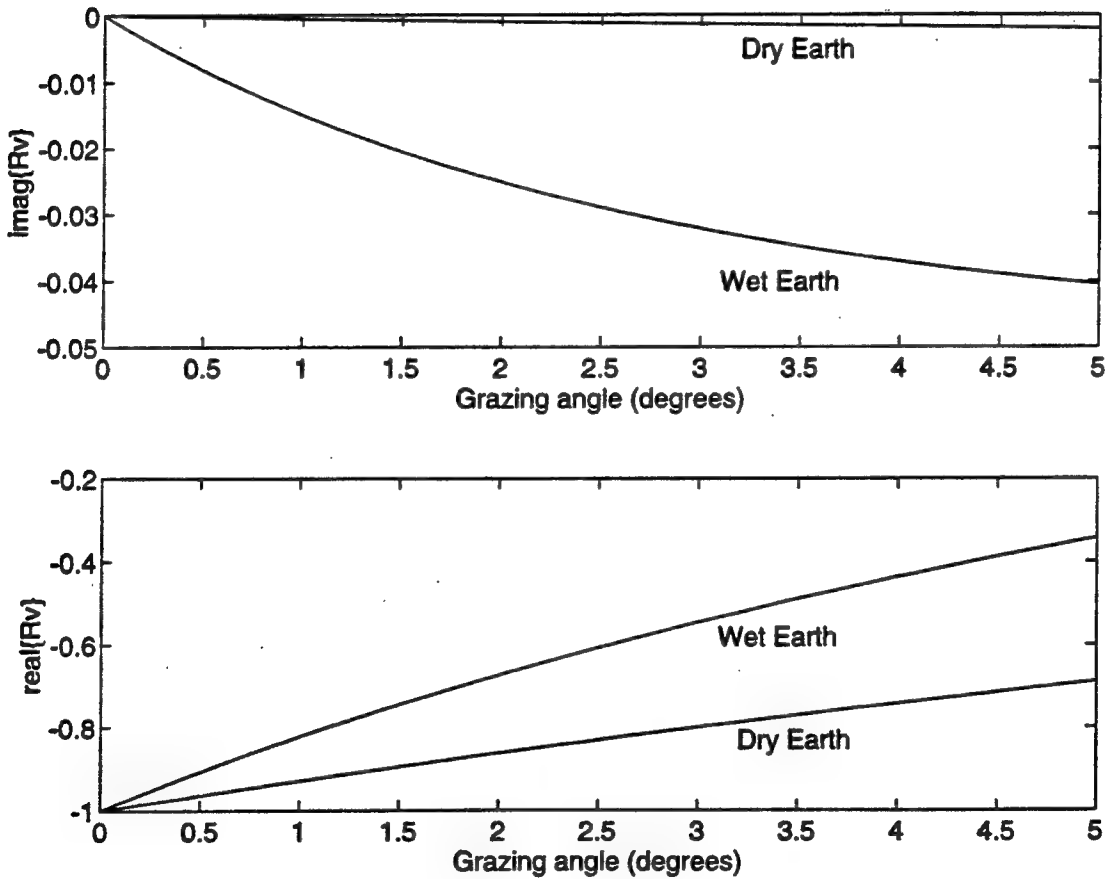


Figure 14: Reflection coefficient versus grazing angle.

The reflection coefficient is a function of several factors. For vertically polarized signals the appropriate expression is given by,

$$R_v = \frac{\epsilon_c \sin \psi - \sqrt{\epsilon_c - \cos^2 \psi}}{\epsilon_c \sin \psi + \sqrt{\epsilon_c - \cos^2 \psi}} \quad (69)$$

where ψ is the grazing angle which can be determined using

$$\psi = \sin^{-1} \left(\frac{h_1 + h_2}{r} \right) \quad (70)$$

and ϵ_c is the complex dielectric constant which can be defined in terms of the dielectric constant ϵ_r and conductivity σ of the reflection surface as [9]

$$\epsilon_c = \epsilon_r - j60\sigma\lambda \quad (71)$$

Figure 14 plots the real and imaginary values of R_v for dry earth and wet conditions.

Considering the assumptions made for r , h_1 , and h_2 the reflection coefficient can be approximated by

$$R_v \approx \frac{2\epsilon_c}{\sqrt{\epsilon_c - 1}} \sin \psi - 1 \quad (72)$$

Substituting the right hand side of equation (70) for ψ and using the resultant expression to replace R_v in equation (68) then

$$s_{rcvr} \approx \frac{s_{dir}}{r} \left(\frac{2\epsilon_c(h_1 + h_2)}{\sqrt{\epsilon_c - 1}} + j \frac{4\pi h_1 h_2}{\lambda} \right) \quad (73)$$

In terms of the transmitted signal s_{tx} (equation (61))

$$s_{rcvr} = \frac{s_{tx}}{r^2} \left(\frac{\lambda\epsilon_c}{2\pi\sqrt{\epsilon_c - 1}} (h_1 + h_2) + j h_1 h_2 \right) e^{-j\frac{2\pi}{\lambda}r} \quad (74)$$

where the fact that $r_0 \approx r$ has been used here. For the frequencies and antenna heights used during the field trials, the above expression for s_{rcvr} is accurate to within 0.2 dB amplitude and 0.3° phase at a range of 1 km, and 4 dB amplitude and 6° phase at a range of 50 m.

The corresponding path loss, l_{earth} can be calculated using

$$l_{earth} = \frac{|s_{rcvr}|^2}{s_{tx}^2} \quad (75)$$

Approximating s_{rcvr} by equation (74), the path loss expression becomes

$$l_{earth} = \frac{|\gamma|^2}{r^4} \quad (76)$$

where

$$\gamma = \frac{\lambda \epsilon_c}{2\pi\sqrt{\epsilon_c - 1}} (h_1 + h_2) - j h_1 h_2 \quad (77)$$

4.5.3 Multipath Model

In examining Figure 13, the signal is reflected off the ground at a single point. In reality, the entire ground contributes to the reflected signal (i.e. each point on the surface can be considered as a point source reradiator). It is the assumption of a smooth uniform infinite earth that leads to a reflected wave which is a mirror image of the incident wave, and therefore allows the use of ray theory.

In most practical situations, the ground will have features which cause it to depart from uniform smooth earth conditions (e.g. terrain features and/or areas with different values of ϵ_c). The result will be a change in the signal which is reradiated from the ground surface of each feature. The approach used here is to consider the reradiated signal from the feature as the sum of a smooth earth component plus a multipath component. The cumulative effects of the smooth earth signals from the entire earth surface can be modelled using the plane earth model and are therefore ignored in the rest of this analysis. It only remains necessary to develop a model for the multipath component.

For simplicity the features which cause a departure from uniform smooth earth conditions are called multipath sources. Since multipath sources are not infinite planes, the reradiation of the signal (multipath component only) from a multipath source will result in some scattering (spreading) of the reradiated wavefront compared to the incident wave. Quantifying this effect is beyond the scope of this report so that only the two extreme scattering conditions are considered: no scattering and isotropic scattering (i.e. the multipath feature acts like an isotropic source). For convenience, a multipath source for which no scattering occurs will be called a *perfect reflector*, and a source which produces isotropic scattering will be called an *isotropic scatterer*. The bearing of the reradiated signal may also be different from that of the incoming signal due to the underlying mechanisms. Although this fact is not overlooked in the following analysis, no attempt is made to quantify this effect.

Figure 15 illustrates the case for a single perfect reflector as viewed from above and the side. This case is nearly identical to the direct signal case, except that the "direct" signal travels from the transmitter to the multipath source (r_a) and on to the receiver (r_b). Viewed from above, the signal path will not be a straight line unless the transmitter, multipath source, and receiver are all aligned. Likewise, the ground reflected signal travels from the transmitter to the ground (r_1), from the ground to the multipath source (r_{2a}), and from the multipath source to the receiver (r_{2b}). Note that in this example, the

reflection point could also have been located on the other side of the multipath source.

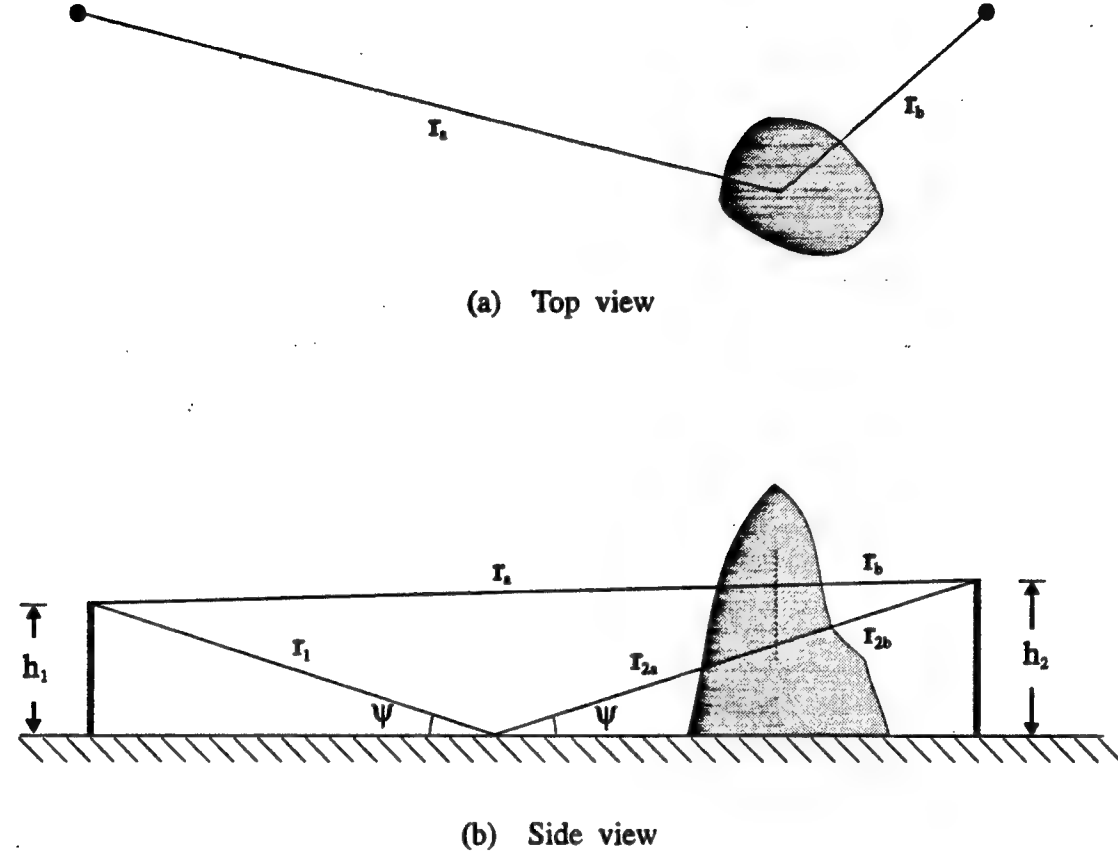


Figure 15: Plane Earth propagation model for a perfect reflector.

The multipath source will delay and attenuate the signals, requiring the introduction of a complex radiation coefficient R_m where $|R_m| \leq 1$. It is assumed here that R_m is identical for both signal components.

Given the similarity between this case and the plane earth model, and using the same assumptions, equations (74) and (76) are easily modified to get

$$s_{mult} = s_{tx} \frac{\gamma R_m}{(r_a + r_b)^2} e^{-j \frac{2\pi}{\lambda} (r_a + r_b)} \quad (78)$$

and

$$l_{mult} = \frac{|\gamma R_m|^2}{(r_a + r_b)^4} \quad (79)$$

It is also useful to compare the path loss in this case to the path loss l_{earth} undergone

by the direct signal. Defining the ratio $l_{excess} = l_{mult}/l_{earth}$ as the excess path loss, then

$$l_{excess} = \left(\frac{r}{r_a + r_b} \right)^4 |R_m|^2 \quad (80)$$

Figure 16 plots the excess path loss as a function of position for the transmitter and receiver separated by 5 km. It is assumed that for each position on the plot the geometry is favourable for the generation of a reradiated signal directed towards the receiver. Since R_m simply scales the results, a value of $|R_m| = 1$ is used. Not surprisingly there is no excess path loss for multipath sources located along the direct signal path with path loss increasing as the position is moved from the direct signal path.

Figure 17 illustrates the case for an isotropic scatterer. Since the multipath feature acts like an isotropic source, the path losses from the transmitter to the multipath source and from the multipath source to the receiver can be treated independently. Hence the received signal is given by,

$$s_{mult} = s_{tx} R_m \left(\frac{\gamma_1}{r_a^2} e^{-j \frac{2\pi}{\lambda} r_a} \right) \left(\frac{\gamma_2}{r_b^2} e^{-j \frac{2\pi}{\lambda} r_b} \right) \quad (81)$$

where

$$\gamma_1 = \frac{\lambda \epsilon_c}{2\pi \sqrt{\epsilon_c - 1}} (h_1 + h_m) - j h_1 h_m \quad (82)$$

$$\gamma_2 = \frac{\lambda \epsilon_c}{2\pi \sqrt{\epsilon_c - 1}} (h_m + h_2) - j h_m h_2 \quad (83)$$

and h_m is the height of the signal path above the ground at the multipath source (shown Figure 17). Simplifying the expression for s_{mult} leads to

$$s_{mult} = s_{tx} \frac{\gamma_1 \gamma_2 R_m}{(r_a r_b)^2} e^{-j \frac{2\pi}{\lambda} (r_a + r_b)} \quad (84)$$

The corresponding path loss equation is given by

$$l_{mult} = \frac{|R_m \gamma_1 \gamma_2|^2}{(r_a r_b)^4} \quad (85)$$

The excess path loss in this case is given by,

$$l_{excess} = \left| \frac{R_m \gamma_1 \gamma_2}{\gamma} \right|^2 \left(\frac{r}{r_a r_b} \right)^4 \quad (86)$$

Figure 18 plots the excess path loss for the same transmitter-receiver geometry and

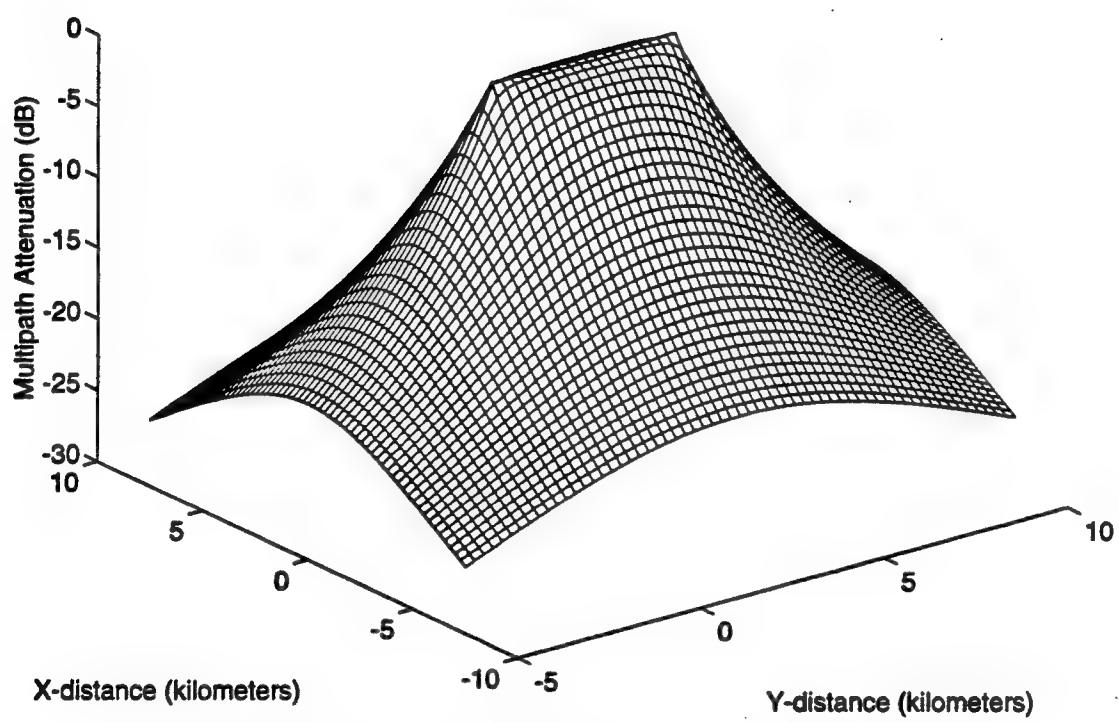
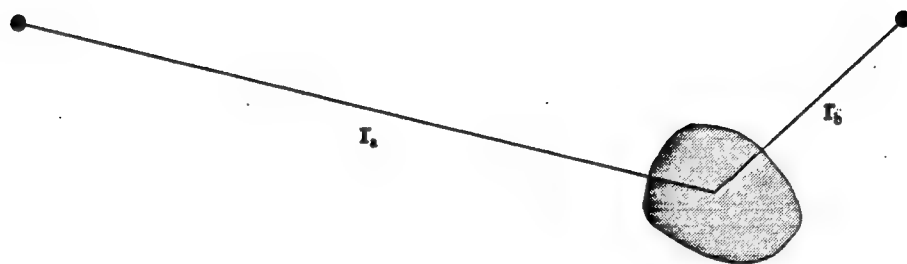
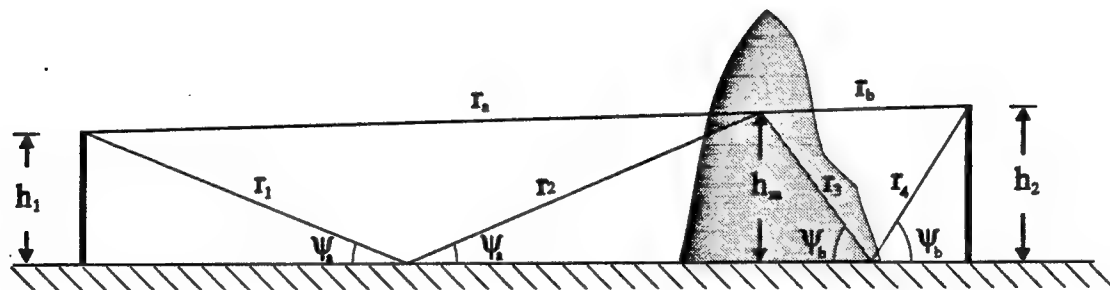


Figure 16: Excess path loss for a perfect reflector.



(a) Top view



(b) Side view

Figure 17: Plane Earth propagation model for an isotropic scatterer.

assumptions as used in Figure 16. The ground conductivity was also assumed to be $\sigma = 3 \times 10^{-4} \text{ Mho/m}$, and the dielectric constant $\epsilon_r = 3$ (dry earth conditions). For simplicity, the center of the scattering source was assumed to lie on the line joining the transmitting and receiving antennas when the horizontal profile is viewed as shown in Figure 17. Accordingly,

$$h_m = \frac{2h_1 h_2}{h_1 + h_2} \quad (87)$$

However, in general, h_m will depend on the size and shape of the feature so that the above expression will not usually be true. For positions corresponding to the transmitter and receiver, it was assumed that there was no excess path loss. Inspection of Figure 18 reveals that in the scattering case the excess path loss increases as a function of the distance from both the transmitter and receiver, not the direct signal path as for the reflector case shown in 16. The loss also increases at a faster rate for the scattering case than for the reflector case.

Before drawing too many conclusions from a comparison of these results, it is worth considering another factor which is important: the direction of the multipath source relative to the transmitter. For example, if the multipath source is aligned with the transmitter and is also located in the farfield of the receiving array, the overall effect will be to change the power of the received signal, but not the relative signal phases and amplitudes measured at the array. Since the bearing estimates depend only on the relative amplitude and phase information, no errors are introduced. If the multipath source is in a different direction than the transmitter, then this will no longer be the case.

In an attempt to quantify this effect, and ignoring all other errors except multipath, a single snapshot of equalized data can be defined as

$$\mathbf{y} = \beta \mathbf{s} + \mathbf{m} \quad (88)$$

where β is the complex signal amplitude, \mathbf{s} is the signal vector defined by equation (12), and \mathbf{m} is the $N \times 1$ vector representing the contribution of multipath. The component of multipath that gives rise to error in the DF estimates is that which is orthogonal to the signal vector \mathbf{s} . Therefore it is useful to redefine equation (88) as,

$$\mathbf{y} = \alpha \mathbf{s} + \mathbf{m}_\perp \quad (89)$$

where α is the apparent signal amplitude given by

$$\alpha = \beta + \mathbf{s}^H \mathbf{m} \quad (90)$$

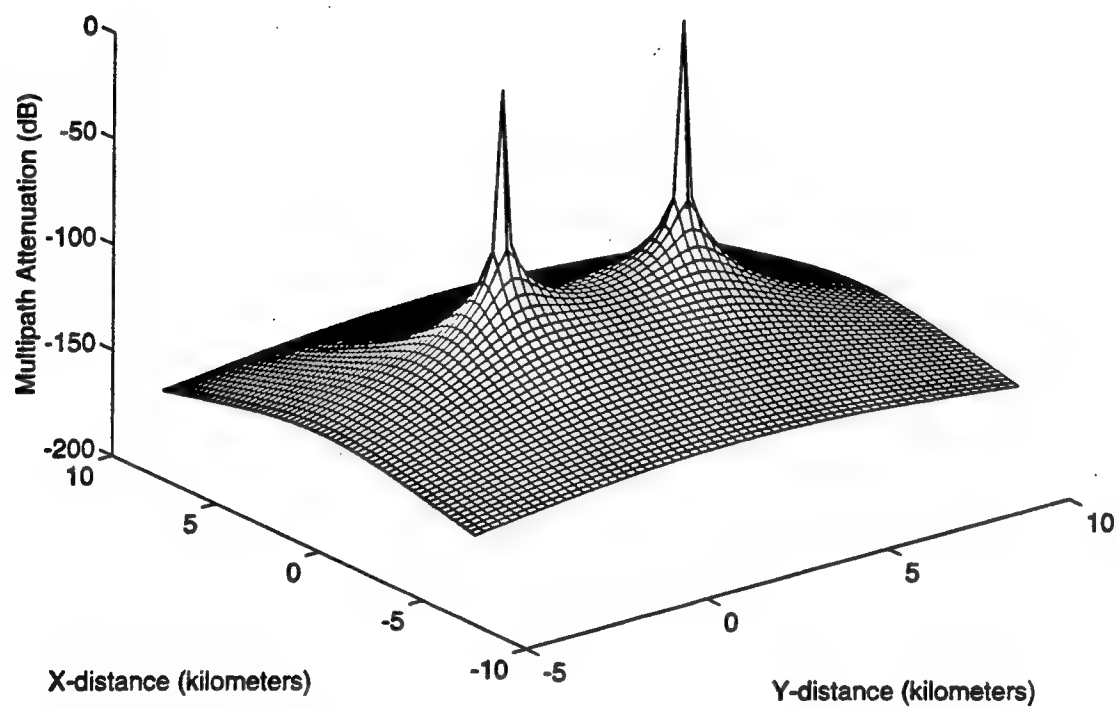


Figure 18: Excess path loss for an isotropic scatterer.

and \mathbf{m}_\perp is the orthogonal component of the multipath such that $\mathbf{s}^H \mathbf{m}_\perp = 0$ and is given by,

$$\mathbf{m}_\perp = \mathbf{m} - \mathbf{s} \mathbf{s}^H \mathbf{m} \quad (91)$$

Defining the loss function l_φ as the ratio of the apparent multipath power to the actual multipath power, and calling this the directional loss function, then

$$\begin{aligned} l_\varphi &= \frac{|\mathbf{m}_\perp|^2}{|\mathbf{m}|^2} \\ &= \frac{|\mathbf{m}|^2 - |\mathbf{m}^H \mathbf{s}|^2}{|\mathbf{m}|^2} \\ &= 1 - |\rho|^2 \end{aligned} \quad (92)$$

where ρ is the complex correlation coefficient given by

$$\rho = \frac{\mathbf{s}^H \mathbf{m}}{|\mathbf{m}|} \quad (93)$$

For a single multipath source in the farfield of the receiving array \mathbf{m} will have the form given in equation (12) except the transmitter bearing ϕ is replaced by the multipath source bearing φ . Under these conditions

$$\rho = \frac{1 - e^{j\frac{2\pi d}{\lambda}(\sin \varphi - \sin \phi)}}{N(1 - e^{j\frac{2\pi d}{\lambda}(\sin \varphi - \sin \phi)})} \quad (94)$$

which simplifies to $\rho = 1$ for $\varphi = \phi$.

The function l_φ is plotted (in dB) in Figure 19 for the same transmitter-receiver geometry used in Figure 19 and assuming the direct signal bearing is $\phi = 0^\circ$. As would be expected, multipath sources approximately in line with the transmitter and receiver have far less effect than sources which are further off the transmitter-receiver line.

It is useful to observe the combined effect of l_φ and l_{excess} for both types of multipath considered. Accordingly, Figures 20 and 21 are repeats of Figures 16 and 18 with the directional effects included. The main difference between Figures 20 and 21 and the originals is the suppression of multipath originating near the transmitter, although this is far more evident in the case of the scattering source of multipath.

Based on these figures some further comments are in order. For example, perfect reflectors are geometry dependent — they illuminate the receiving array for a very limited subset of transmitter bearings and ranges. The result is that the DF bearing error for one transmitter bearing will be completely unrelated to the error occurring at another

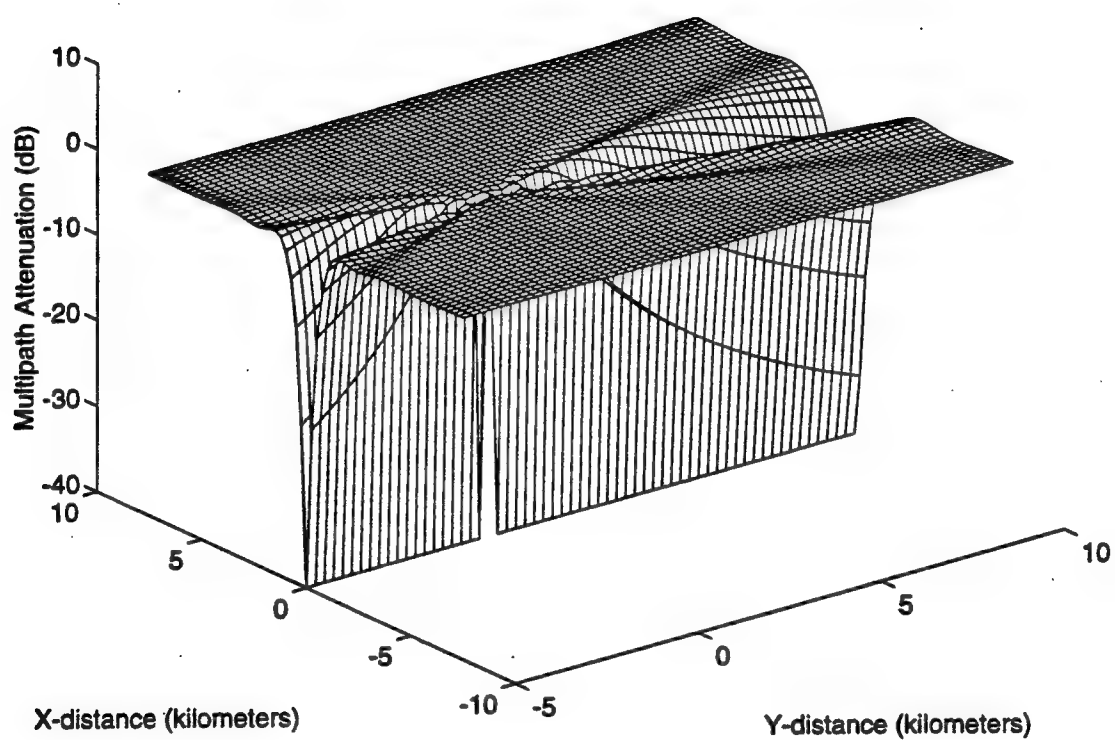


Figure 19: Directional multipath power loss l_φ .

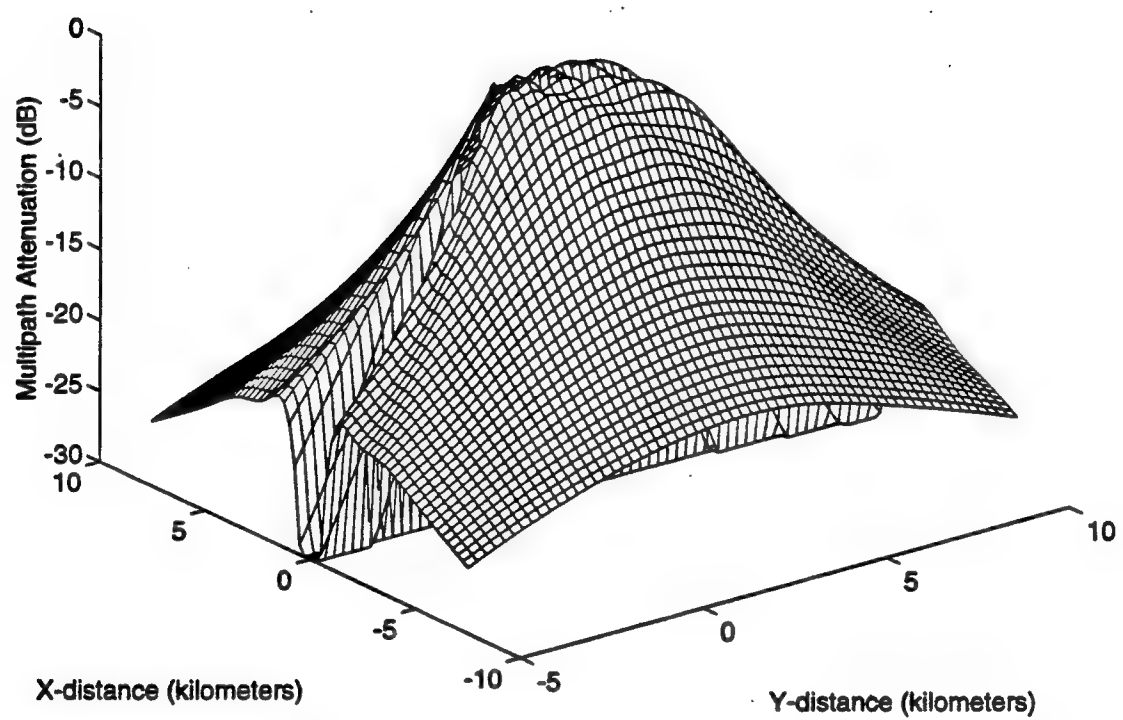


Figure 20: Combined effect of excess path loss and directional loss for a perfect reflector.

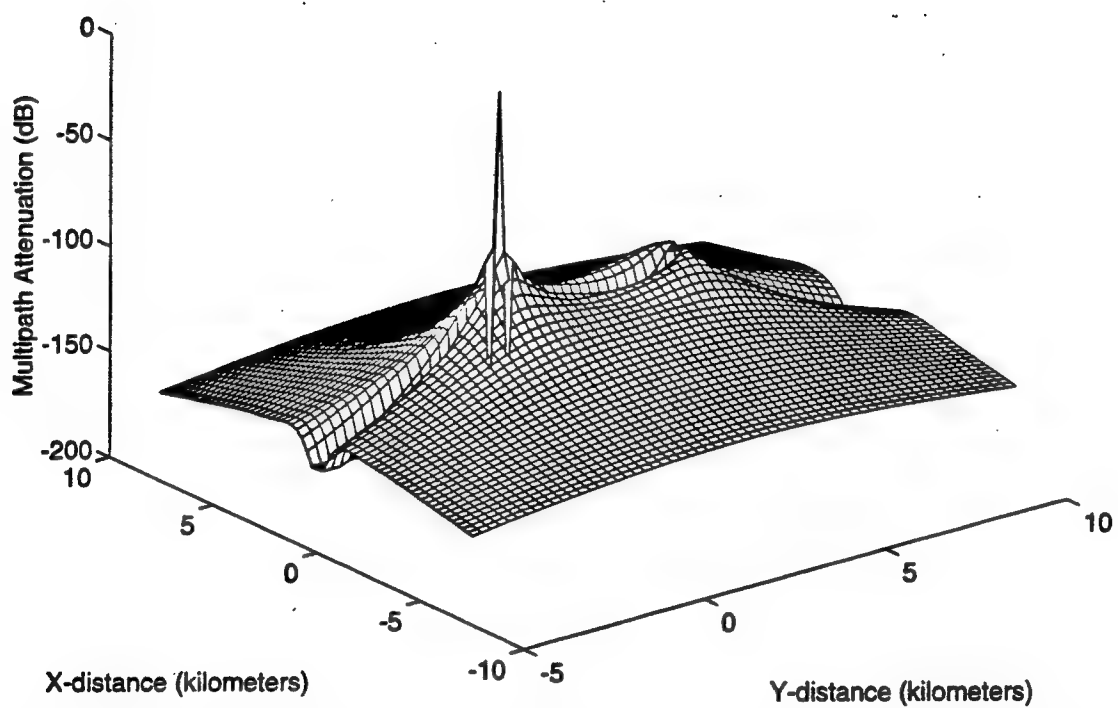


Figure 21: Combined effect of excess path loss and directional loss for an isotropic scatterer.

bearing. This effect is illustrated in Figure 22 where the DF error response for the Osprey system (after broadside normalization as defined in equation (35)) has been simulated for a single signal and three multipath sources at equal ranges. Each source was assumed to illuminate the receiving array only when $\varphi_m - \phi = 10^\circ$, where m is the multipath source designation (1, 2, or 3). The three plots show the effect of increasing the distance between the receiver and the multipath sources from 10 meters to 1000 meters. Note that the results at close range are unrealistic in the sense that a perfect reflector will have infinite size which implies near field conditions, i.e. simple ray tracing will not be valid. However the results do provide a reasonable indication of the effects of both range and bearing.

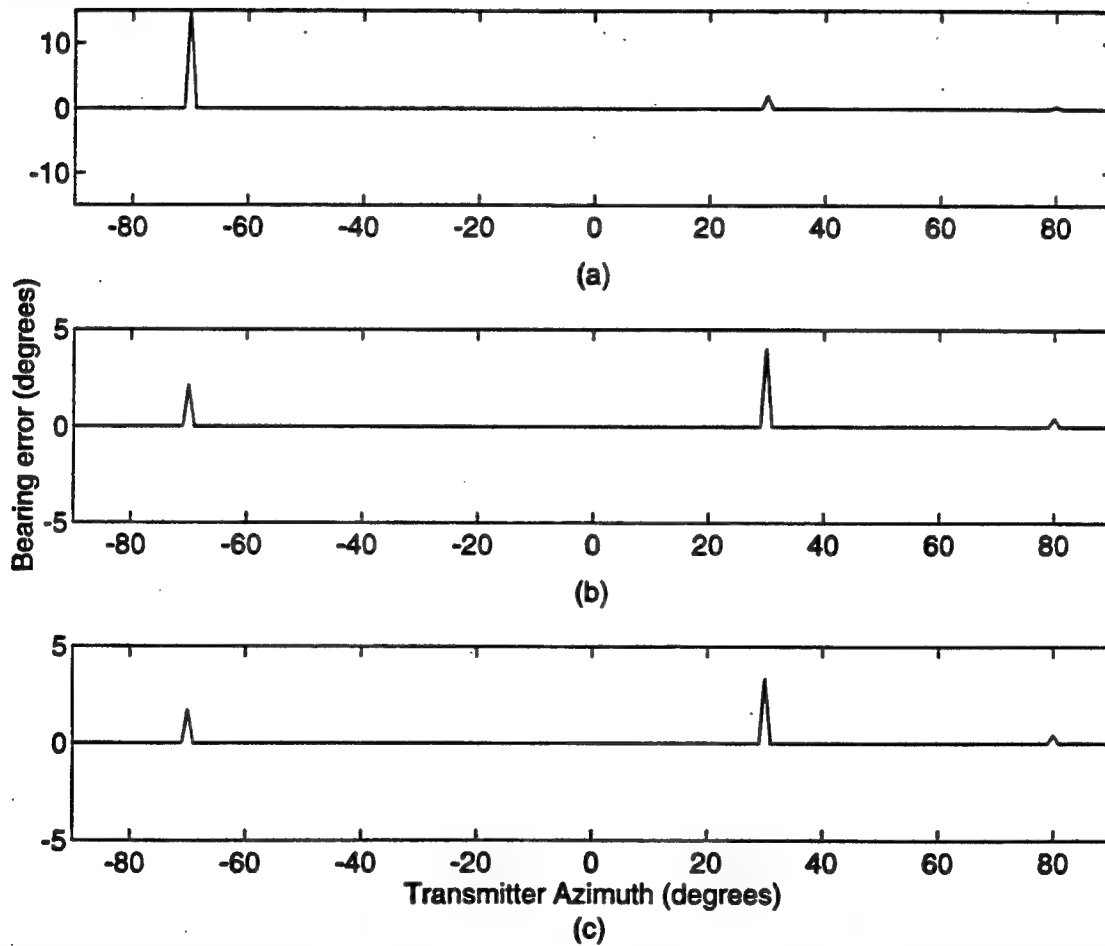


Figure 22: Simulated DF error response for 3 multipath reflectors at bearings of -60, 40, and 90 degrees, and ranges of (a) 10 m (b) 100 m, and (c) 1000 m.

Examining the plots in Figure 22, the effects of the individual multipath sources are clearly identifiable (at $\phi = -70, 30$, and 80 degrees) and uncorrelated. Range does not

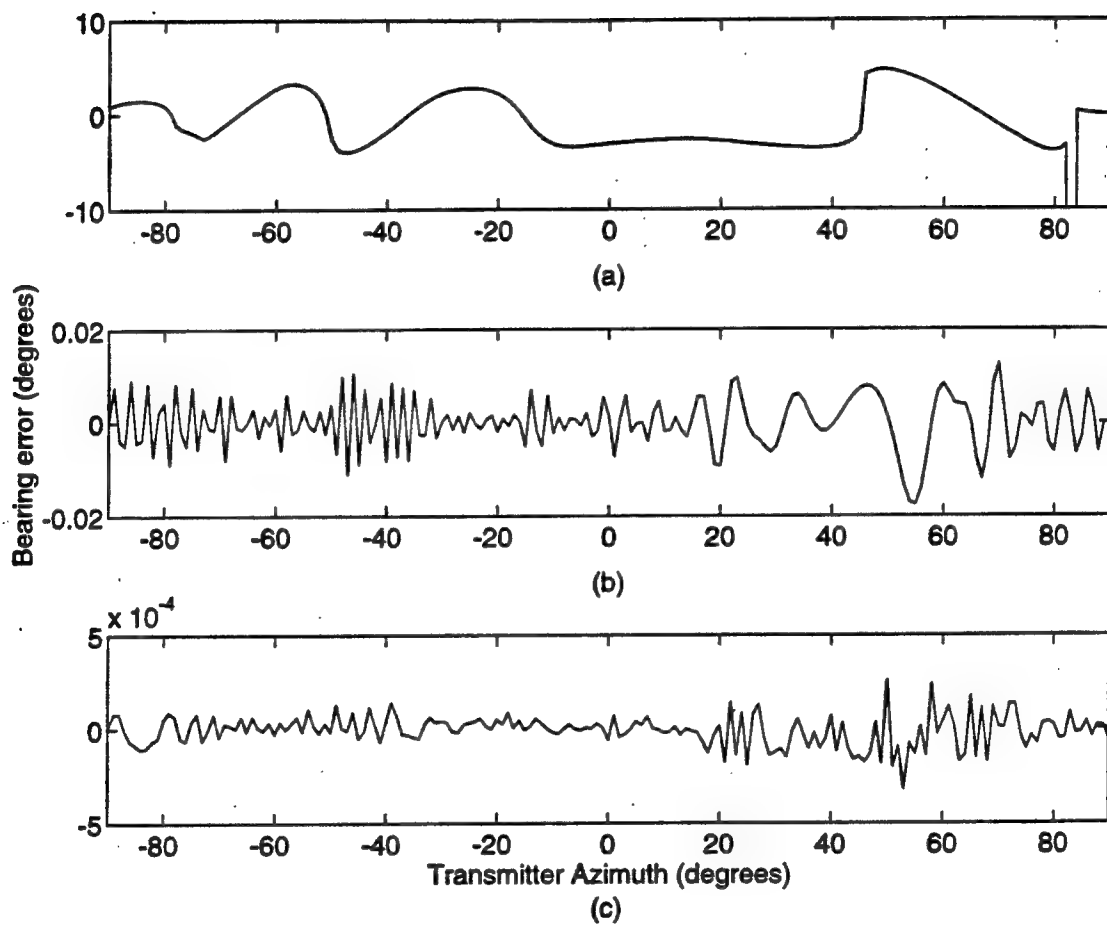


Figure 23: Simulated DF error response for 3 multipath scatterers at bearings of -60, 40, and 90 degrees, and ranges of (a) 10 m (b) 100 m, and (c) 1000 m.

appear to have any significant effect. Extrapolating these results to a greater number of multipath sources would result in a very noise-like error pattern with no correlation between the error at any one bearing compared to any other bearing. The implication is that if a large number of reflector like sources dominate the multipath environment, then calibration of the array response will be very difficult, i.e., incremental measurements will be required over the complete spectrum of transmitter azimuth angles and ranges of interest to achieve any significant accuracy improvement compared to equalization.

Isotropic scattering sources are not dependent on the bearing of the incident signal but are affected by the path lengths involved. The strongest multipath components will tend to originate near the receiving antenna. If the transmitter is moved, the multipath environment will not significantly change. As a result, characterizing the site around the receiving array may be sufficient in order to significantly improve DF performance. Examples of this are shown in Figure 23 which is identical to Figure 22 except that the multipath sources completely scattered the signal. In this example it is clear that multipath effects are localized to the area near the receiving array and diminish rapidly with range. Additionally, since the error pattern is affected at all azimuth angles, this implies a high degree of correlation between measurements taken at different azimuth angles. A final observation is that the error pattern becomes more noise-like as the range increases, thus providing one way of distinguishing multipath effects from mutual coupling effects.

5.0 RESULTS

The DF results for all four data sets are shown plotted in Figures 24-27. In each figure the top plot shows the bearing measurements $\hat{\phi}$ (dots) and map bearing ϕ (solid line) in degrees as a function of the measurement number. The measured results have been corrected for the directional ambiguities inherent in the antenna array (i.e. a linear array cannot distinguish between the two angles ϕ and $180^\circ - \phi$). The middle plot shows the bearing error $\hat{\phi} - \phi$ (in degrees). The lowest plot shows the bearing error (in degrees) after broadside normalization (defined in equation (35)).

5.1 Error Analysis

The RMS error for each of the data sets displayed in Figures 24-27 is given in Table 1 for both the unnormalized and broadside normalized cases. Inspection of the figures shows that the unnormalized results are dominated by the errors that occur for bearings towards endfire ($\pm 90^\circ$), especially for the data sets collected in March. By contrast, the

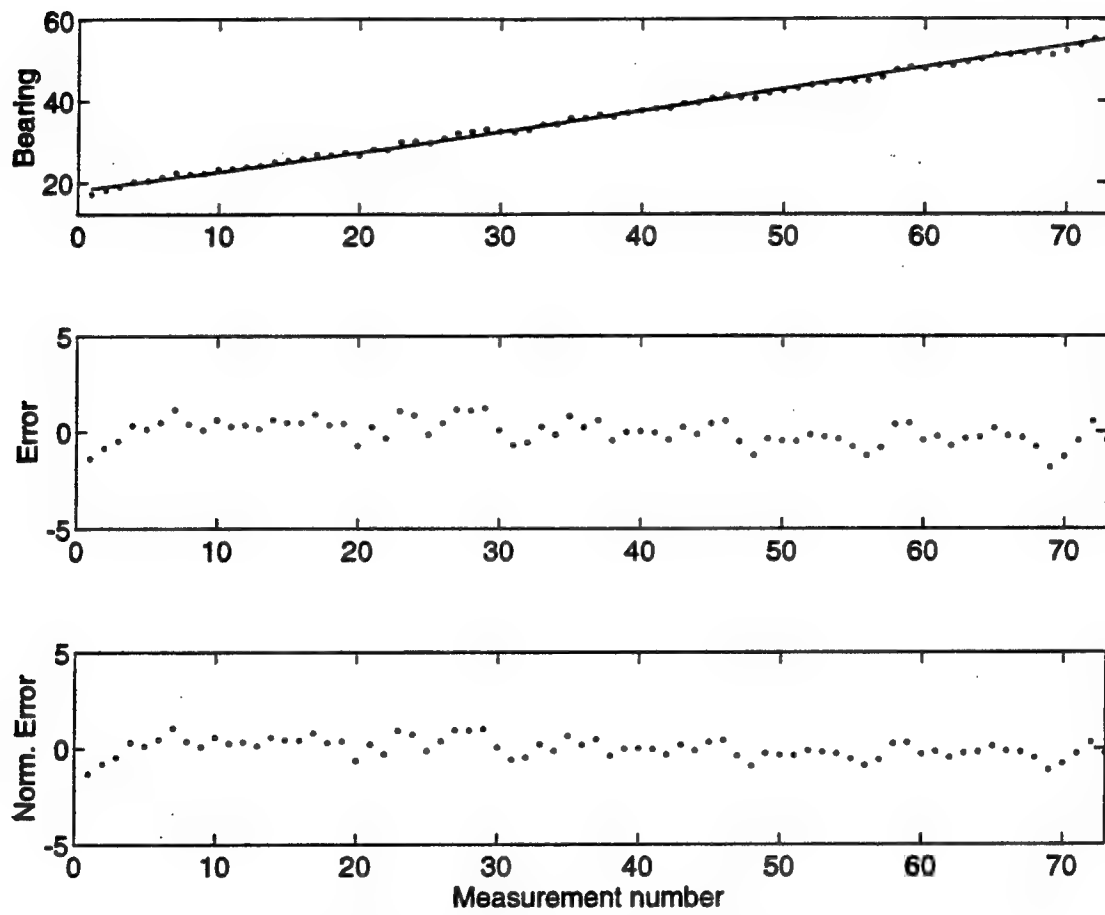


Figure 24: Field trial results for November 5, 1992

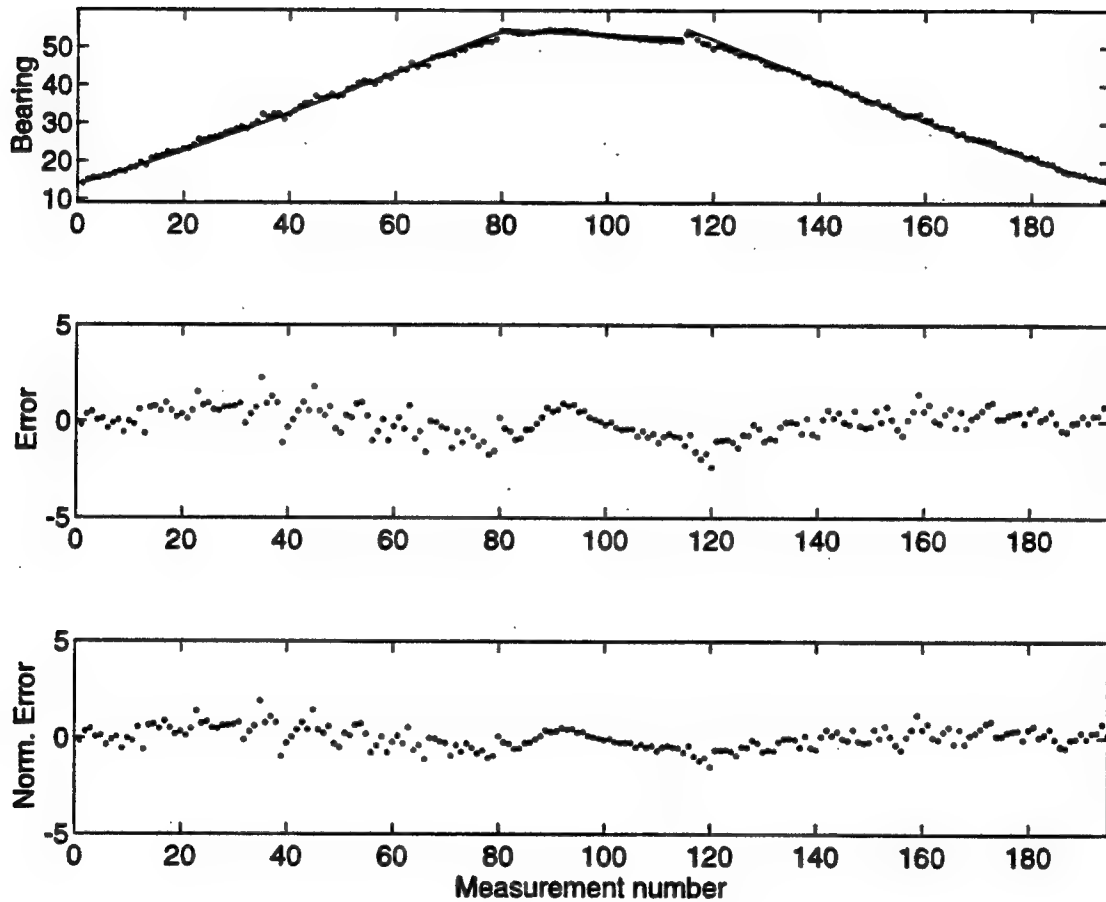


Figure 25: Field trial results for November 6, 1992

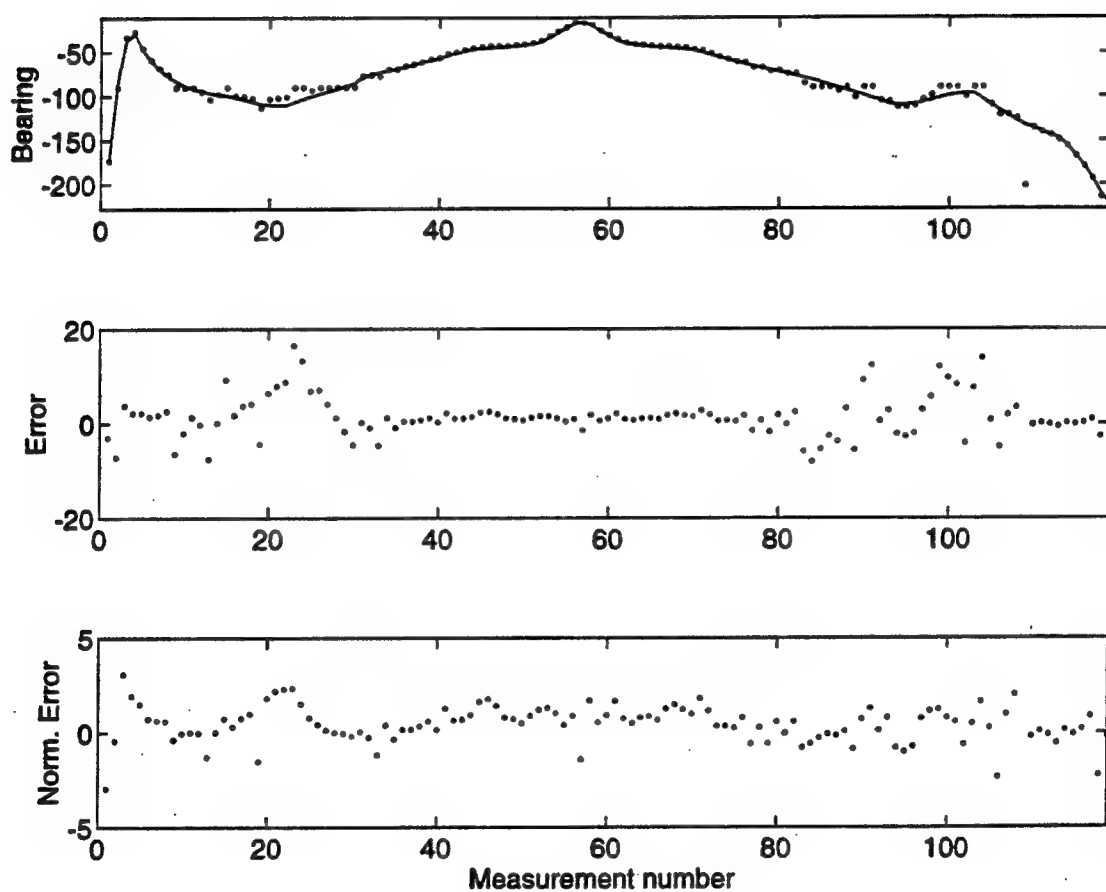


Figure 26: Field trial results for March 24, 1993

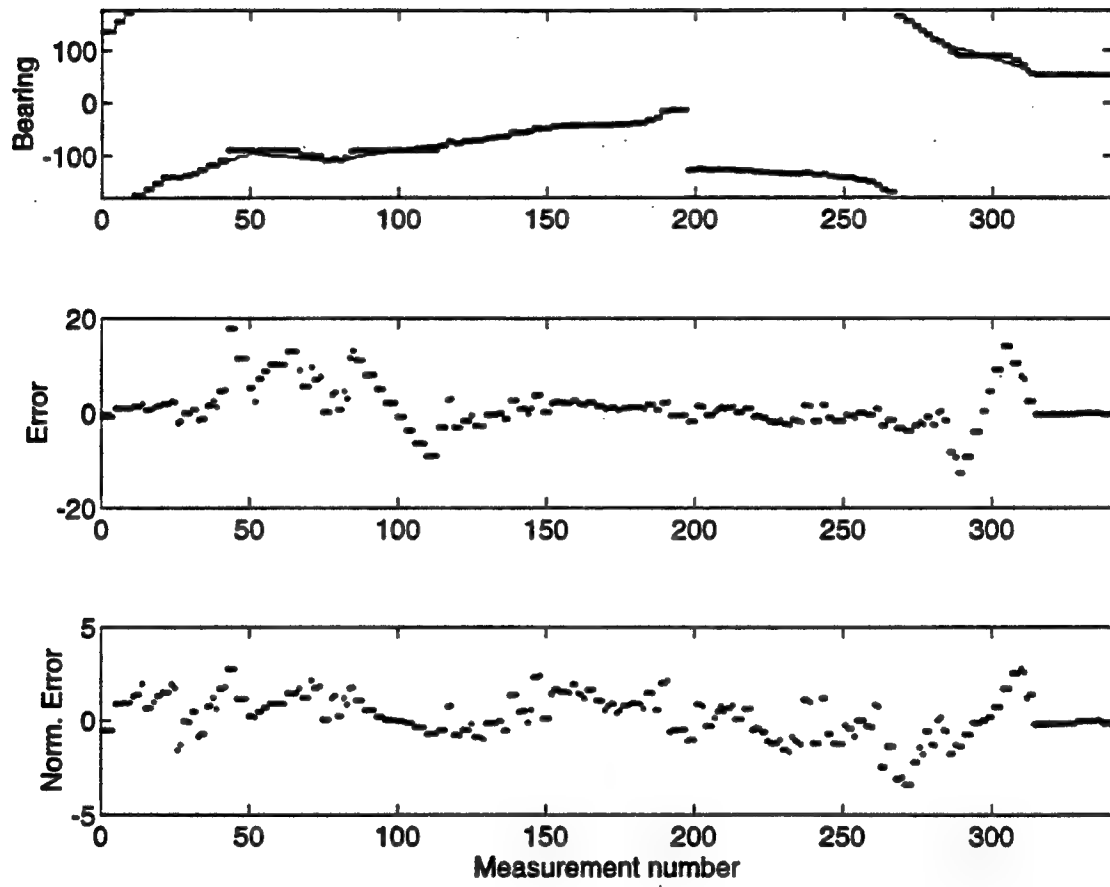


Figure 27: Field trial results for March 25, 1993

normalized results exhibit far less dependency on DF antenna array geometry making this representation of the errors more suitable for analysis. Therefore the remaining discussion of the results deals with the broadside normalized results only.

In the next three sections, the error results are broken down into temporal effects, spatial effects excluding multipath, and multipath effects. Figures 28-31 show the corresponding range and signal to noise ratios for the field trial measurements which are relevant to the following analysis. The broadside normalized error (which was shown in Figures 24-27) is also shown for reference.

The bearing error for measurement 109 on March 24 is discussed in more detail under multipath effects.

5.1.1 Temporal Effects

Temporal effects include noise, wind effects, and receiver drift. Noise and wind effects can be quantified based on the analysis presented in Section 4. Receiver drift can be quantified based on the measurements as will be discussed shortly.

From Figures 28c-31c the signal to noise power ratio was normally than 40 dB in most of the DF measurements during the field trials. The associated RMS bearing errors given by equation (39), which ignores the wind effects and receiver drifts was therefore less than 0.1° and can be considered insignificant compared to the RMS error values listed in Table 1. In the few cases where the signal to noise power ratio was less than 40 dB (e.g. measurements 9, 10, 79, and 80 in Figure 30c), these measurements can be ignored.

To minimize wind induced bearing errors, calm days (i.e. windspeed less than 10 km/h) were chosen for the field trials. On these days the position error of the antennas in the DF array was less than 1 cm. This translates to a maximum RMS bearing error of 0.1° which indicates wind effects can be ignored.

To validate the noise and wind results, 27 repeated DF measurements spanning a period of 3.5 minutes were taken for the last transmitter position on March 25. The

Table 1: RMS Error Summary of Field Trial Results

Data Set	RMS Error	Normalized RMS Error
Nov 5	0.64	0.51
Nov 6	0.72	0.54
Mar 24*	4.44	1.06
Mar 25	4.84	1.15

* Bearing error for measurement 109 excluded

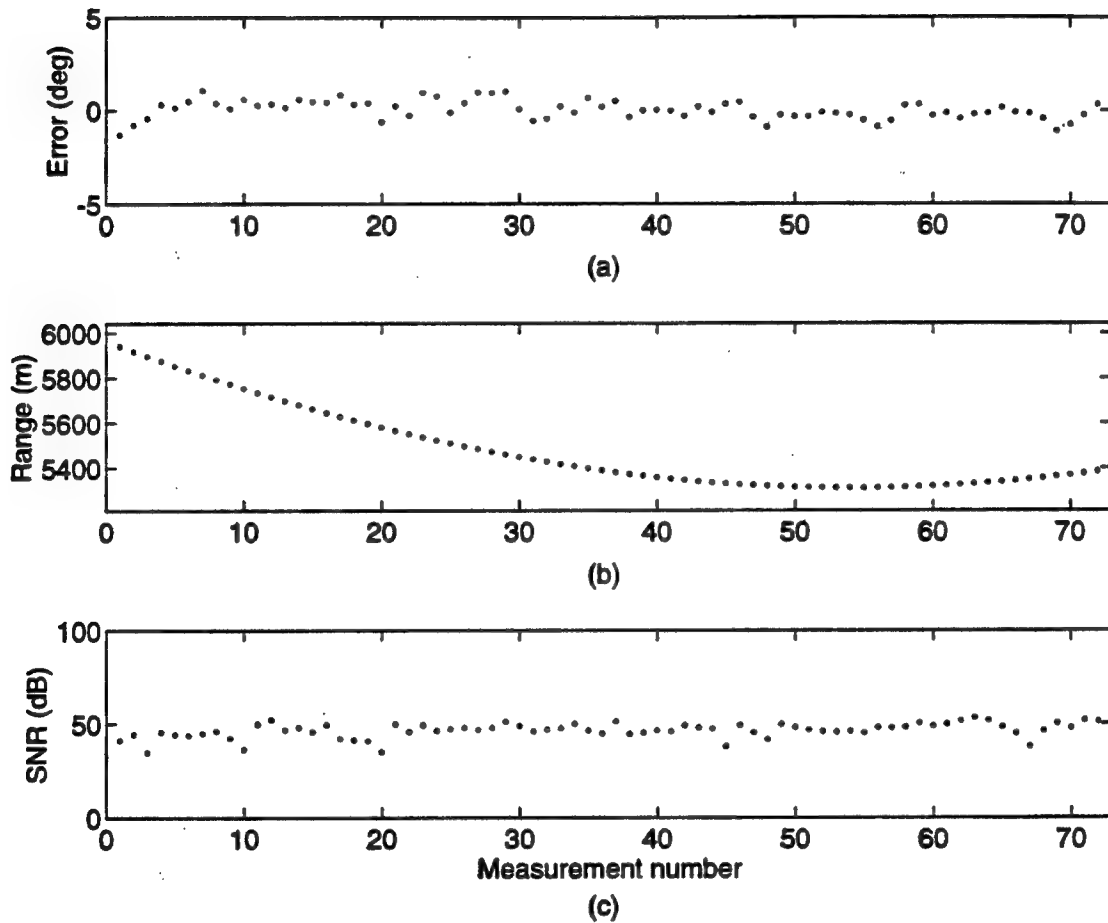


Figure 28: Field trial parameters for November 5, 1992: (a) broadside normalized error, (b) range, and (c) signal to noise ratio.

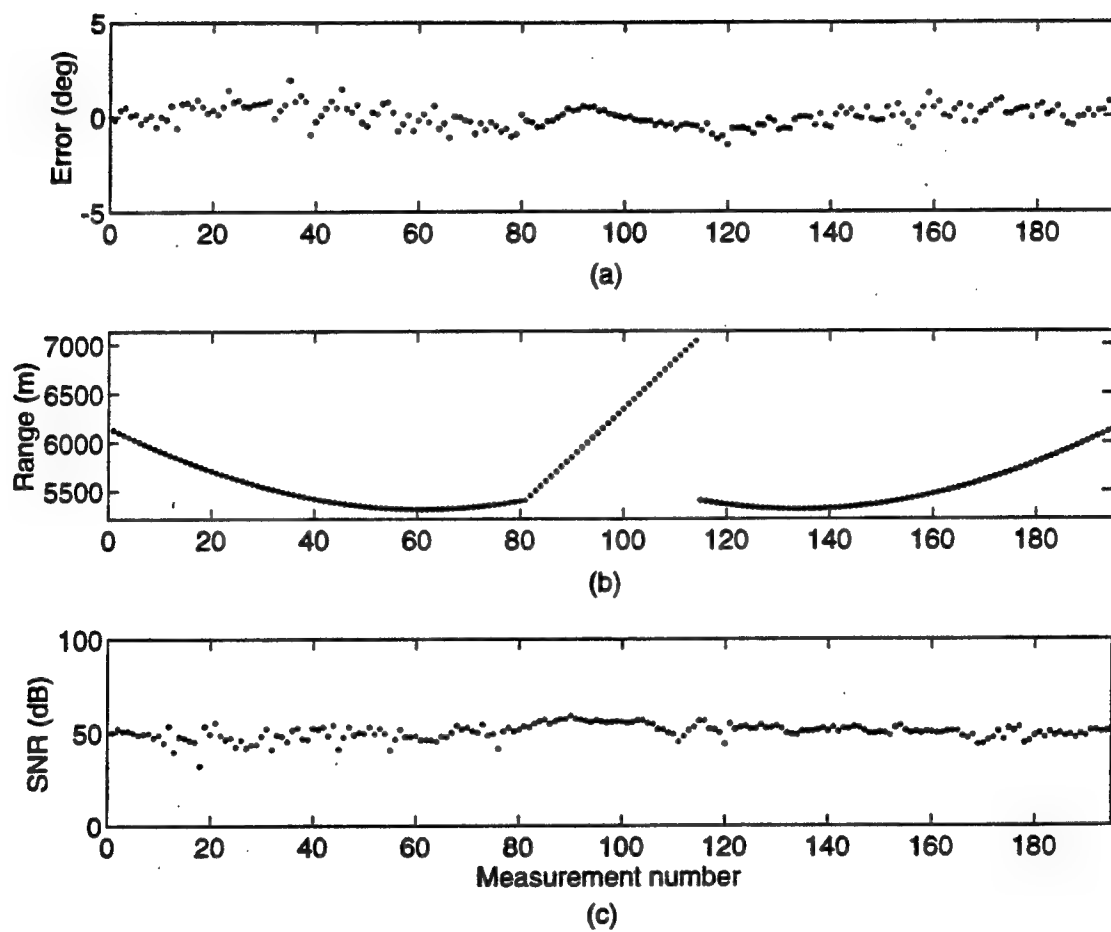


Figure 29: Field trial parameters for November 6, 1992: (a) broadside normalized error, (b) range, and (c) signal to noise ratio.

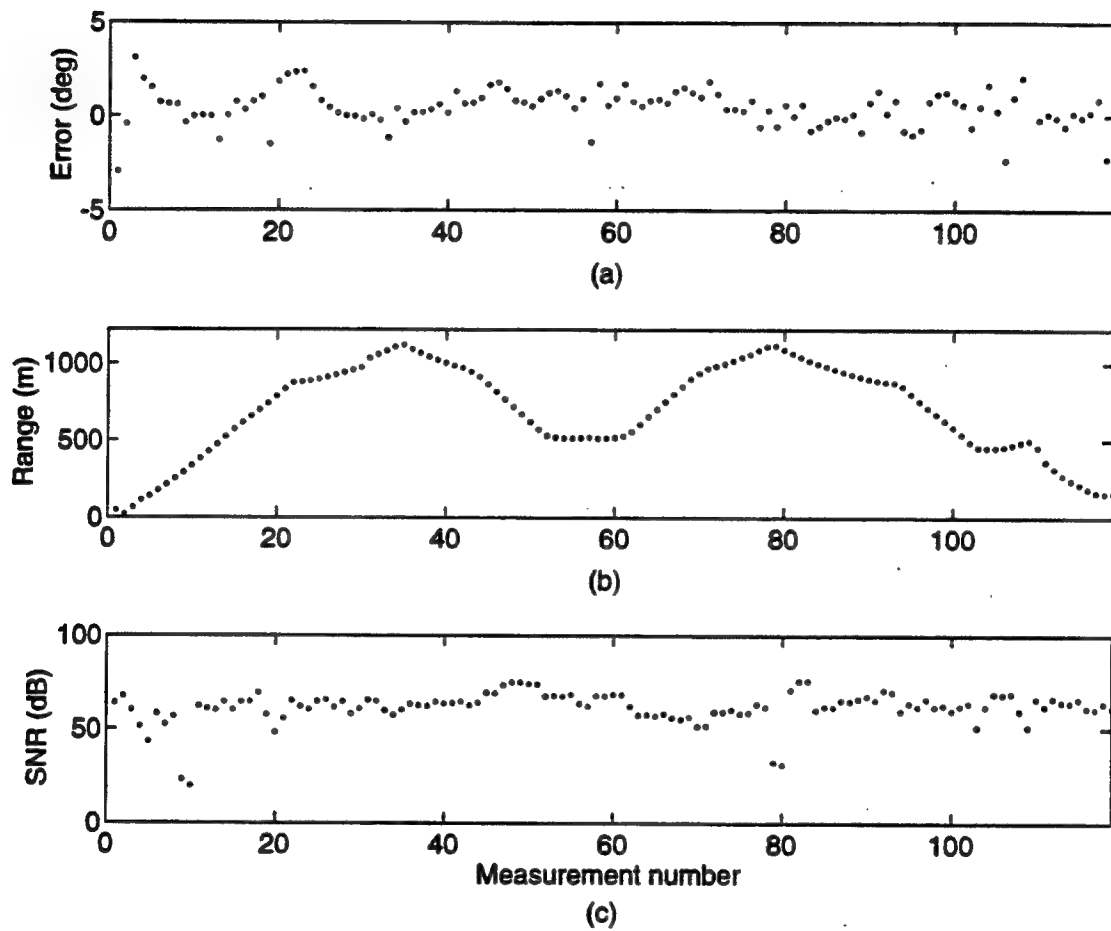


Figure 30: Field trial parameters for March 24, 1993: (a) broadside normalized error, (b) range, and (c) signal to noise ratio.

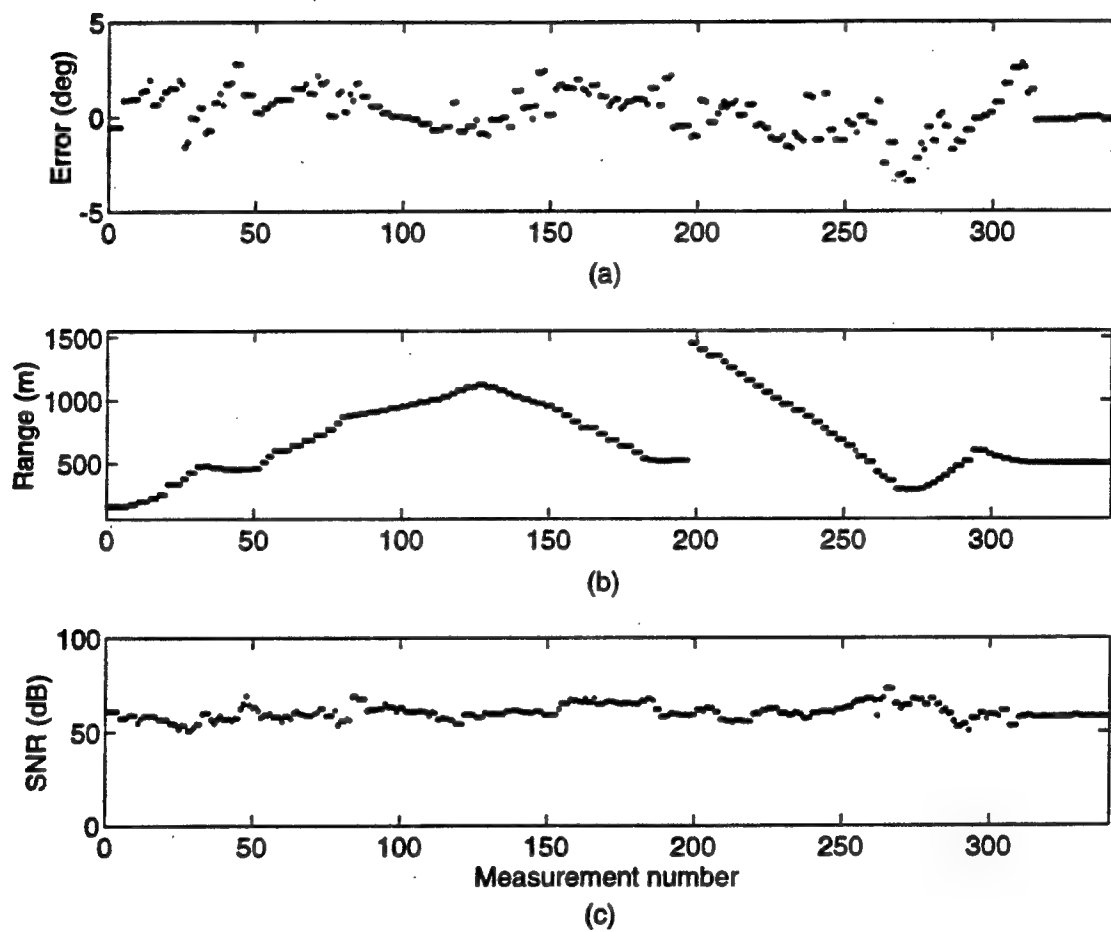


Figure 31: Field trial parameters for March 25, 1993: (a) broadside normalized error, (b) range, and (c) signal to noise ratio.

standard deviation in these results was 0.08° supporting the conclusion that, for high signal to noise power ratios (> 40 dB) and low winds (< 10 km/h), the noise and wind induced errors were insignificant.

Tests of the Osprey receivers in the lab found them to be very stable when properly warmed up with phase drift rates of less than $0.1^\circ/12$ hours. Although this implies insignificant drift in the DF results, given that the drift tests were done under constant temperature conditions, the lab results don't guarantee stable operation in the field. To test whether any significant drift occurred during the measurements, the complex gain coefficients were estimated from data collected for the same positions (or nearly the same positions) but at different times, and the results compared. There are two groups of 3 data subsets, for a total of 6 subsets, in which positions were repeated. These subsets are summarized in Table 2 with subsets A, B, and C representing one group of positions, and subsets D, E, and F representing the second group of positions. The time column in Table 2 refers to the time of the middle measurement of the subset (i.e. the mean time).

Table 2: Data Subsets for Drift Estimation

Subset	Date	Time	Measurement No.	Comment
A	Nov 5	15:34:55	all	see Figure 3
B	Nov 6	12:16:50	1-81	same as A (see also Figure 4)
C	Nov 6	13:26:53	115-195	same as A except in reverse order
D	Mar 24	13:31:55	13-56	(x_{E-W}, y_{N-S}) positions starting at (50, -472) to (-495, -143) in Figure 5
E	Mar 24	14:16:49	57-102	same as D except in reverse order
F	Mar 25	10:39:33	52-197	same as D (see also Figure 4)

The estimated gains and phases for each of the subsets are listed in Tables 3 and 4. Inspection of these results would suggest that during same day measurements, phase and gain drifts did occur, with a maximum phase drift of up to 8° (Table 3, channel 2) and gain drift of up 13% (e.g. Table 3, channel 4). These values are substantially greater than what would have been predicted from the lab tests. However, since the phase and gain estimates have been constrained according to equations (8) and (9), the results in Tables 3 and 4 do not necessarily reflect the true drifts. For example, since all the channel phases are referenced to channel 0, a change in the phase offset of channel 0 will appear as a constant phase change in all the other channels. For this reason interpreting the results in this form may be misleading.

Additionally, to observe drift effects in more detail, DF measurements were taken over periods of several days with the transmitter at close range and in a fixed position. This

led to the identification of equipment problems (i.e. shielding problems which had no effect on the results of the other experiments) which were subsequently fixed. Although it was not possible to run another properly controlled drift test for this report, preliminary testing indicates that the environment may cause daily phase variations on the order of a few degrees. However, until further tests can be performed to confirm this, it has been assumed that the equipment was the sole cause of the drift effects.

Table 3: Channel Phase Drift during Field Trials in November

Channel	θ_A	θ_B	θ_C	g_A	g_B	g_C
0	0.0	0.0	0.0	0.74	0.86	0.88
1	98.2	104.7	104.7	1.02	1.01	1.02
2	44.1	48.6	49.3	0.94	0.95	1.03
3	101.2	102.1	110.1	1.40	0.94	0.97
4	-167.2	-161.3	-161.0	0.95	1.17	1.04
5	158.6	171.1	170.9	1.17	1.30	1.25
6	-88.0	-75.3	-75.2	0.57	0.44	0.45
7	118.4	122.0	118.3	1.00	1.12	1.16

Table 4: Channel Phase and Gain Drift during Field Trials in March

Channel	θ_D	θ_E	θ_F	g_D	g_E	g_F
0	0.0	0.0	0.0	0.92	0.91	0.88
1	-44.6	-42.7	-46.4	1.01	1.01	1.10
2	-35.1	-35.2	-39.1	1.05	1.05	0.94
3	-60.2	-59.3	-65.8	0.71	0.71	0.72
4	-72.6	-68.6	-75.9	1.16	1.20	1.25
5	-23.6	-21.1	-27.0	1.36	1.36	1.28
6	-5.2	-3.3	-9.4	0.73	0.71	0.77
7	-14.5	-10.8	-12.6	0.89	0.87	0.90

To provide a better idea of the effects of drift, it is simpler to observe the error that is introduced into the DF results. Mathematically the effects of drift on a single snapshot of data z can be represented by

$$z = Dy \quad (95)$$

where D is an $N \times N$ diagonal drift matrix and y represents the calibrated data. The diagonal elements of the drift matrix, d_0, d_1, \dots, d_N , represent the change in the complex gain coefficients of the corresponding channels. The effect on DF estimation can therefore

Table 5: Bearing Errors (in degrees) due to Phase and Gain Drift

Subset	Bearing Error
A	-0.38
B	0.00
C	-0.17
D	-0.17
E	0.00
F	-0.16

be observed by comparing the bearing estimates determined using \mathbf{y} and \mathbf{z} . Additionally if \mathbf{y} represents a single signal with a bearing of 0° , then the value of the bearing estimate for \mathbf{z} will represent the bearing error due to drift.

Using subsets B and E as references for each group, the diagonal elements of the drift matrix \mathbf{D} were calculated for each subset based on the differences between it and the appropriate reference subset. For example, for subset A

$$d_k = \frac{g_{Ak}}{g_{Bk}} e^{j(\theta_{Ak} - \theta_{Bk})} \quad (96)$$

where k represents the channel number. Computing \mathbf{z} for each subset assuming \mathbf{y} represented a signal with a bearing of 0° and no noise, the estimated bearings were determined using MUSIC and tabulated in Table 5. Although these results are limited, they indicate that for same day measurements the effect of receiver drift on the bearing estimates was less than 0.2° . This provides some confidence that receiver drift, although significant, was not a major contributing error during the field trials. For consecutive day results the drift rate was less than $0.4^\circ/\text{day}$, thus providing a further indication that drift was not a major factor during measurements performed on the same day.

5.1.2 Spatial Effects

Two sources of spatial error are considered here, namely, transmitter position errors, and mutual coupling. Both effects can be quantified based on the analysis presented in Section 4.

Uncertainty in the transmitter position degrades the accuracy in the determination of the transmitter bearings from the map, especially as the transmitter gets closer to the DF array. During the November trials ranges varied from 5.3 to 7.0 km. The associated RMS map bearing errors (calculated using equation (21)) ranged from 0.03° to 0.02° RMS, which is significantly less than the overall RMS bearing error values listed in Table 1.

Table 6: Simulated Bearing Errors due to Mutual Coupling

Data Set	Without Equalization	With Equalization
Nov 5	0.37	0.19
Nov 6	0.39	0.23
Mar 24	0.73	0.68
Mar 25	0.67	0.67

Therefore for the November trials, errors in the map bearing estimates were assumed to be negligible. During the March trials, ranges were much shorter and varied from 22.4 m to 1.4 km. The associated RMS map bearing errors were 7.3° to 0.15° . The larger RMS errors are clearly significant. However, by restricting analysis to measurements collected for ranges of 400 m or more, the resultant error in the map bearing estimates ($< 0.2^\circ$) can be ignored.

In the case of mutual coupling the predicted error based on assuming perfect matching, and plotted in Figure 11, was 0.5° RMS. This clearly is significant. To determine whether the theoretical effects predicted were actually observed during the field trials, the curve from Figure 10 has been replotted in Figure 32 along with the DF results from March 25. In this case the directional ambiguities inherent to the linear antenna array were not corrected leaving the bearings restricted to the range -90° to $+90^\circ$. Inspection of the results shows that there is a very good correlation between the actual and theoretical results.

Given these good results, the mutual coupling simulation was run for the same transmitter directions and frequencies used in the actual trials. The RMS error results are tabulated in Table 6 in the middle column. Not surprisingly, the March results, which had a greater number of measurements of signals in the endfire direction, show greater errors than the November results. The stochastic calibration method was also applied to the simulated data to determine the combined effect of mutual coupling and equalization. The results are also tabulated in Table 6 with the November data showing the greatest benefit from equalization. Based on these results, it seems prudent to treat measurements of signals in the endfire direction with some caution.

5.1.3 Multipath Effects

To minimize the effects of the error sources discussed in the previous two sections, the measurement data was reprocessed. Measurements were rejected if the signal to noise ratio was < 40 dB, or the transmitter range was < 400 m. Imposing this criteria resulted in

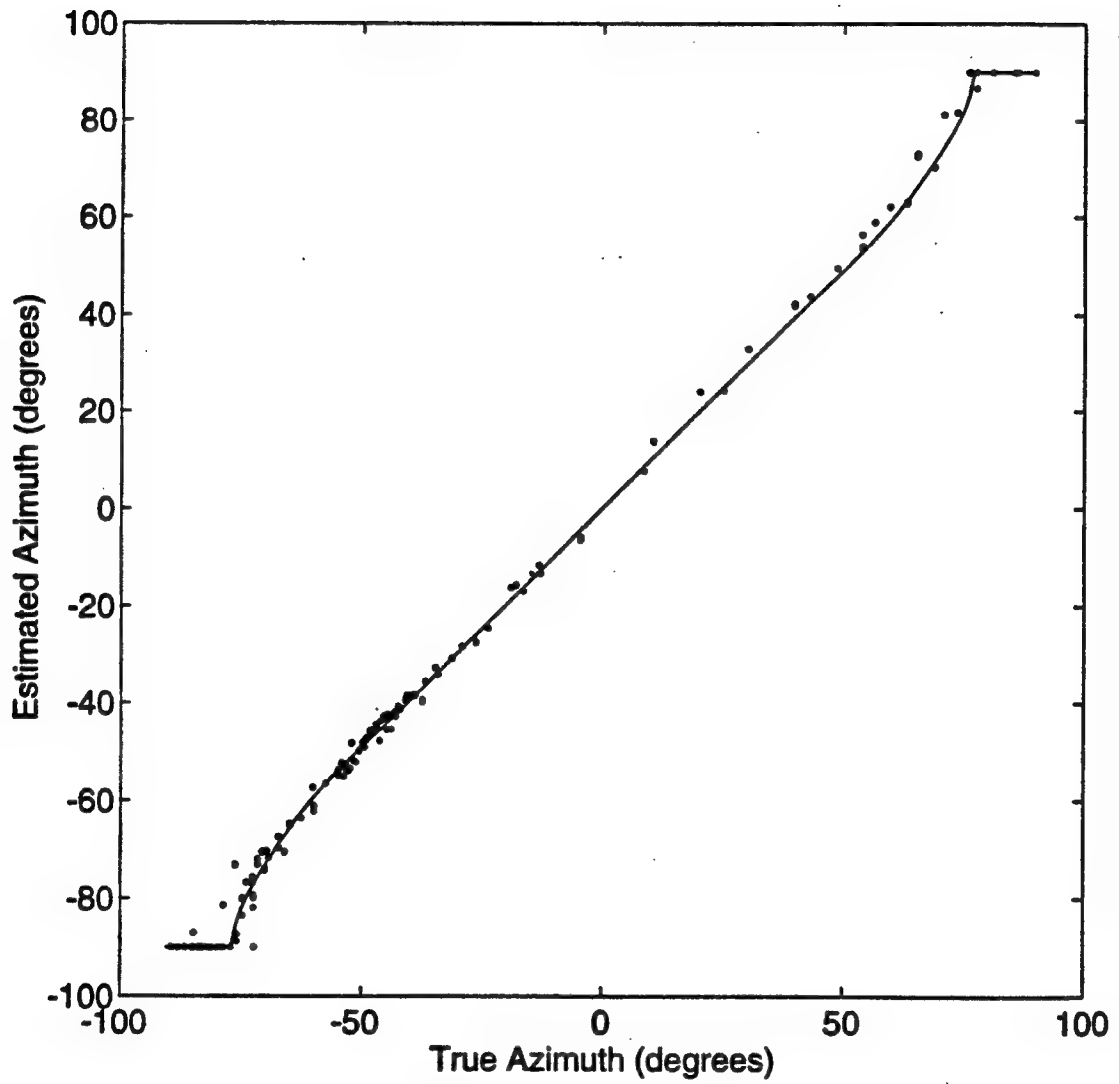


Figure 32: Theoretical mutual coupling effects (solid line) compared to results from March 25, 1993 (dots)

Table 7: RMS Error Summary of Field Trial Results with Mutual Coupling Effects Removed

Data Set	RMS Error
Nov 5	0.47
Nov 6	0.47
Mar 24*	0.84
Mar 25	0.80

* Bearing error for measurement 109 excluded

2% of the November measurements being discarded and 16% of the March measurements being discarded. The error results are shown in Figures 33-36 and are plotted as a function of azimuth. For reference the theoretical effects of mutual coupling have also been plotted.

In general, the bearing errors follow the same trend as the predicted mutual coupling error curves except with a certain amount of scatter. There are, however, a number of exceptions. In Figure 34 an interesting feature occurs between 52° and 55° azimuth. This feature resulted when the transmitter turned the corner on Riddell Road (see Figure 4) and began moving almost directly away from the DF array with a slightly decreasing azimuth bearing. The result was a repeat of some of the azimuth angles already measured but for different ranges. The resultant error in this case appears to be range dependent. This is the kind of effect that would be expected from multipath, particularly if the multipath source produces very little scattering (i.e. more like a perfect reflector than an isotropic scatterer).

In Figure 35 measurement 108 is not shown due to the large bearing error (-68°). During this measurement the transmitter was behind a small building. This seems to be the clearest case of multipath given that the direct signal path was blocked.

In Figures 36 there are several places ($\phi = -130^\circ, -43^\circ$, and 54°) where the error changes by up to 2° over a narrow range of azimuth angles. Again, the most likely cause being multipath.

The amount of scatter observed for each of the measurement sets can be quantified by subtracting the predicted mutual coupling errors from the actual errors. This has been done and the RMS error results tabulated in Table 7. Given the magnitude of the RMS errors, it would appear that multipath was the dominant contributor since all other known error mechanisms have essentially been ruled out.

Finally, in comparing the November and March error results, the scatter in the March errors is also almost twice that of the November errors. The reason for the larger scatter could be due to any number of reasons which may have effected the multipath conditions.

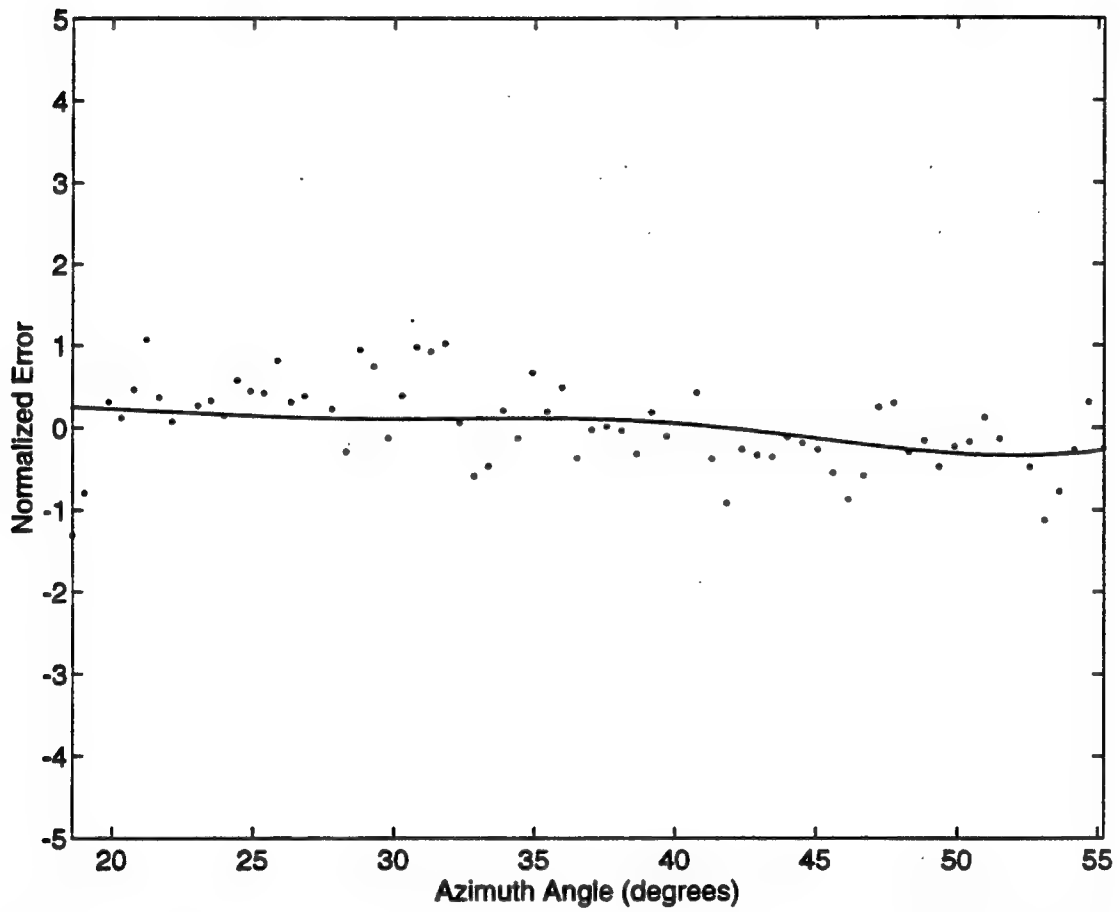


Figure 33: Revised error results for November 5, 1992. The dots represent actual error and the solid line represents predicted error due to mutual coupling.

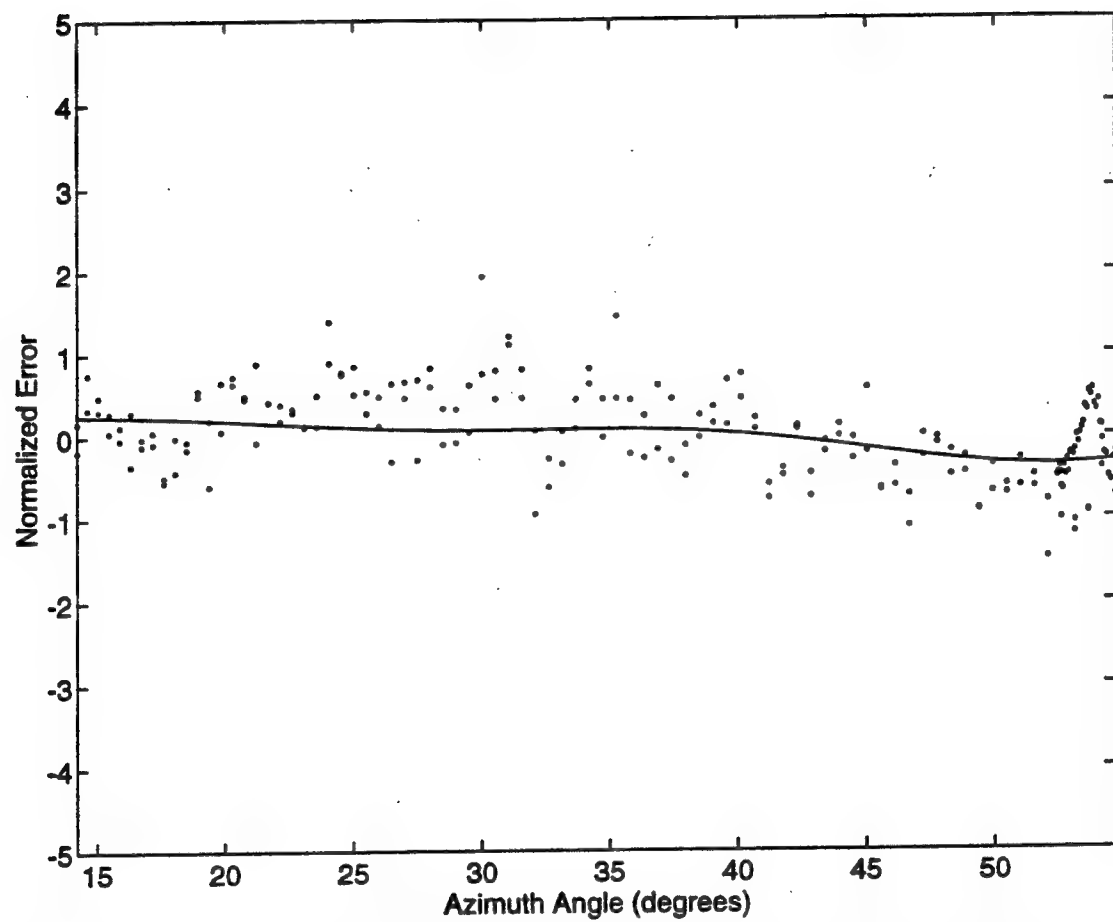


Figure 34: Revised error results for November 6, 1992. The dots represent actual error and the solid line represents predicted error due to mutual coupling.

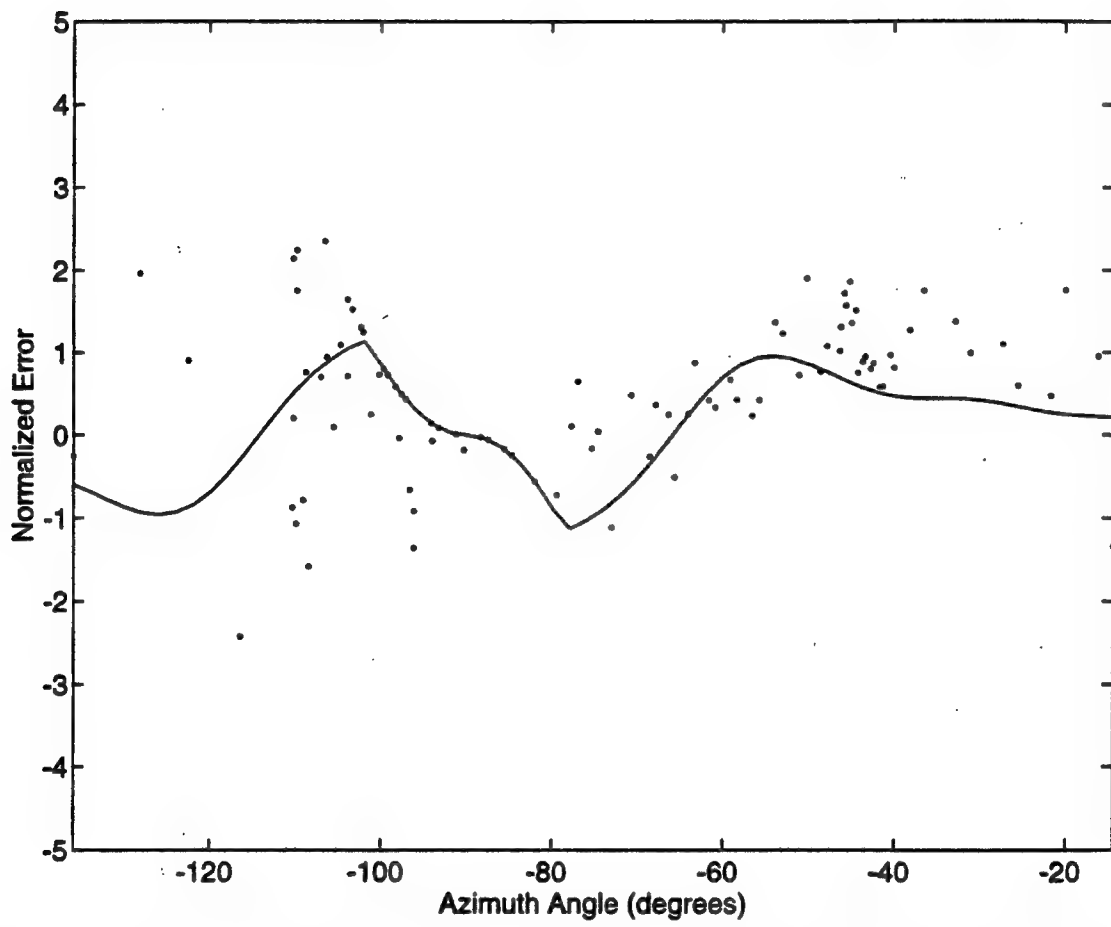


Figure 35: Revised error results for March 24, 1993. The dots represent actual error and the solid line represents predicted error due to mutual coupling.

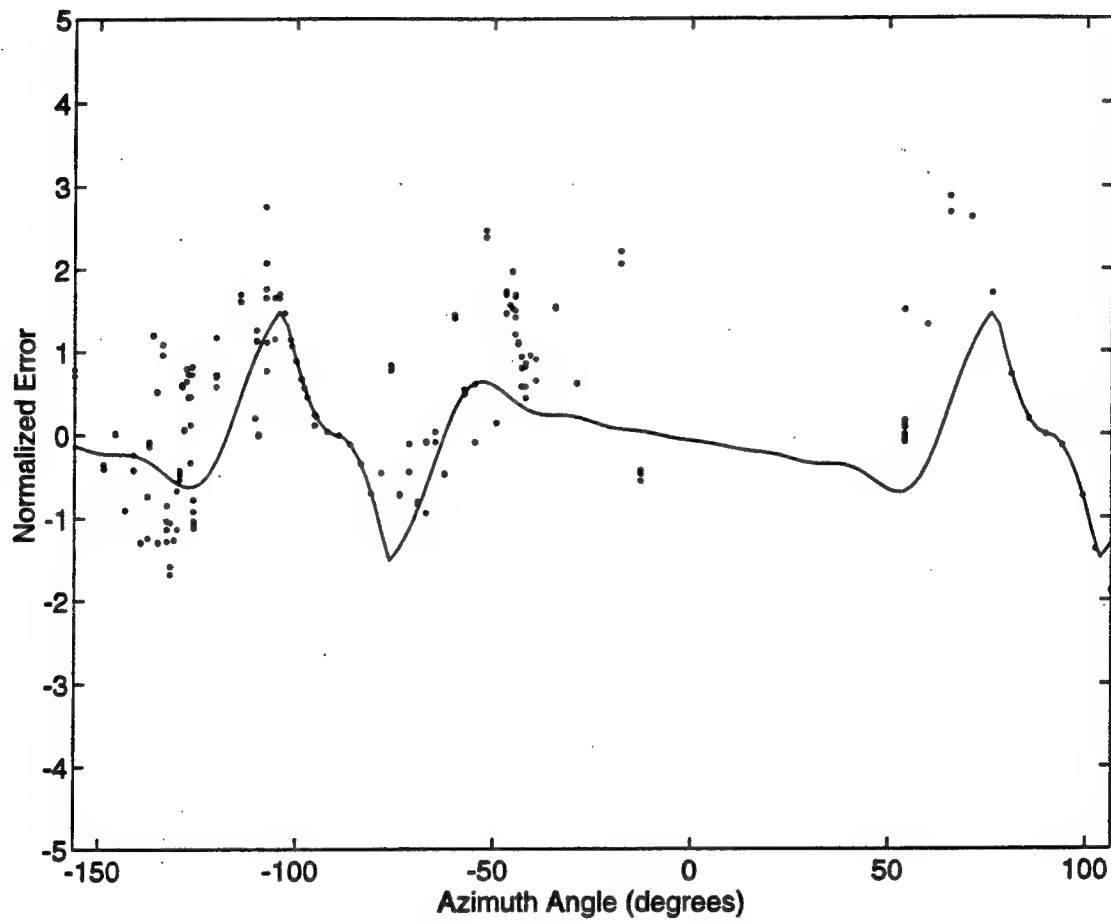


Figure 36: Revised error results for March 25, 1993. The dots represent actual error and the solid line represents predicted error due to mutual coupling.

This includes different environmental conditions, different frequencies, different ranges, and different azimuth angles. In terms of environmental conditions, the ground state may have had an impact on the results obtained during the field trials. For example, in November the ground was wet while in March it was frozen and covered with snow. These differences would be expected to cause differences in the amplitude and phase of the ground reflected signal and possible differences in the measured bearings for the same transmitter positions. Changing the transmitter frequencies would not be expected to change the amount of scatter in the error results. However, this possibility cannot be completely ruled out until further tests are done. Based on the multipath models developed in this report, shorter transmitter ranges might be expected to increase the scatter by increasing the relative contribution of multipath generated near the transmitter (i.e. the loss function l_s has less effect at short range). Finally the signals received during the November trials traversed the field where Osprey system was located from the West. In this direction, there are relatively few prominent physical features for several hundred meters. By comparison, the equivalent distances for the March trials were considerably less. For example, at $\phi = 270^\circ$ a ditch and row of bushes was located within a few meters of the array.

6.0 CONCLUSIONS

This report discusses and analyzes the results of field trials carried out to investigate environmental effects, in particular multipath, on an experimental eight-channel VHF DF system (Osprey). The theoretical effects of error mechanisms which degraded the DF measurements were analyzed in detail including modelling of the multipath environment. This analysis was then used to break down the measurement errors in terms of these mechanisms. The RMS error results for the March 1993 trials (which generally reflect the worst case results) are shown in Table 8. These results have been normalized to reflect accuracy for a signal at 0 degrees azimuth.

Quantitatively, multipath propagation was found to be the greatest source of error followed closely by mutual coupling. Based on the modelling studies of both phenomena, important qualitative differences were found. Mutual coupling errors are a function of transmitter azimuth only (when a plane wave signal is considered) and are predictable. The error pattern changes relatively slowly cycling once from the maximum positive error to the maximum negative error over a range of 180 degrees in azimuth. Multipath errors are a function of both transmitter azimuth and range. The error pattern becomes more unpredictable (noise-like) as the range of the multipath source from the DF system

increases (at a range of 0 meters multipath and mutual coupling can be regarded as the same phenomena). These qualitative differences make it relatively easy to distinguish mutual coupling effects from multipath effects.

In examining the multipath induced errors, two important observations were made. The first was that the multipath errors were very noise-like, indicating that significant multipath sources ranged up to several hundred meters or more. The second was there appeared to be a transmitter range dependency even for transmitter ranges over 5 km. Based on the theoretical models, this implies that sources of multipath which were reflective in nature (i.e. redirect the incident signal in a new direction with limited scattering) were significant.

These last two observations lead to complications for site calibration if improved DF accuracy is the objective. They indicate that calibration of the array steering vector (or array manifold) at a particular frequency needs to be performed as a function of both range and azimuth, not azimuth as is usually done. Further experimentation will be required to verify these observations before any definite conclusions can be drawn.

Drift effects (i.e. changes in the gain and phase matching of the DF receiver channels) were also observed which were probably due to the equipment, but may have also been due to changes in the multipath environment. Further experimentation will be required to verify whether the environment is a factor.

In general the results described in this report indicate that the multipath environment is very complex. Modelling can be used, with some success, to better understand the statistical effects of multipath. For future work, the theoretical models need to be refined to better approximate real life effects. Further field testing will also be required to verify the models and determine appropriate model parameters (e.g. density of multipath sources, relative importance of reflective versus scattering types, etc.). This could ultimately lead to the development of new approaches to VHF DF including (but not restricted to) new algorithms and new calibration techniques.

Table 8: RMS Error Summary

Mechanism	RMS Error (degrees)
Transmitter Position	0.2
Noise	0.1
Wind	0.1
Equipment Drift	0.2
Mutual Coupling	0.7
Multipath	0.8

REFERENCES

- [1] "Navaids and Avionics Enroute Systems, Doppler VHF/DF, Site Selection", Publication No. C4-2VHF/DF-3, Telecommunications and Electronics Branch, Transport Canada, March 1, 1976.
- [2] Schmidt, R.O., "Multiple Emitter Location and Signal Parameter Estimation", *IEEE Transactions on Antennas and Propagation*, vol. 34, no. 3, pp. 276-280, March 1986.
- [3] Pillai, S.U., and Kwon, B.H., "Performance Analysis of MUSIC-Type High Resolution Estimators for Direction Finding in Correlated and Coherent Scenes", *IEEE Transactions on Acoustics, Speech, and Signal Processing*, vol. 37, no. 8, pp. 1176-1189, August 1989.
- [4] Friedlander, B., "A Sensitivity Analysis of the MUSIC Algorithm", *IEEE Transactions on Acoustics, Speech, and Signal Processing*, vol. 38, no. 10, pp. 1740-1751, October 1990.
- [5] Stoica, P., and Nehorai, A., "MUSIC, Maximum Likelihood, and Cramer-Rao Bound", *IEEE Transactions on Acoustics, Speech, and Signal Processing*, vol. 37, no. 5, pp. 720-741, May 1989.
- [6] Wong, K.M., Walker, R.S., and Rieggoda, G., "Effects of Random Sensor Motion on Bearing Estimation by the MUSIC Algorithm", *IEE Communication, Radar, and Signal Processing*, vol. 135, Part F, no. 3, June 1988.
- [7] Kraus, J.D., "Antennas", McGraw-Hill Book Company, 1950.
- [8] Brown, G.H., and King, R., "High-Frequency Models in Antenna Investigations", *Proceedings of the Institute of Radio Engineers*, vol. 22, no. 4, pp. 457-481, April 1934.
- [9] Shigekazu, S., "A Basic Atlas of Radio-Wave Propagation", John Wiley and Sons, 1987.

APPENDIX

A.0 Stochastic Calibration Method

In the stochastic model, multipath is assumed to be completely unpredictable and can be modelled as a spatially white Gaussian process. The array response equation for this case is discussed in Section 3.2 and given by equation (10) which is reproduced here as,

$$\mathbf{A}^{-1}\mathbf{X} = \mathbf{S}\mathbf{B} + \mathbf{N} \quad (\text{A.1})$$

Given that the errors produced by multipath are represented by \mathbf{N} , then a least squares solution for \mathbf{A} and \mathbf{B} could be determined by minimizing the total multipath error power given by $\text{trace}(\mathbf{N}^H\mathbf{N})$. This is not optimal, however, as the errors represented by \mathbf{N} are not spatially white since the power of the multipath signals are proportional to the signal power. Therefore, a strong signal would be expected to produce larger errors than a weaker signal. To whiten the multipath noise it is necessary to normalize the noise according to the signal power, i.e., multiply the k^{th} column of \mathbf{N} by b_k^{-1} . Accordingly, equation (A.1) becomes

$$\mathbf{A}^{-1}\mathbf{X}\mathbf{B}^{-1} - \mathbf{S} = \mathbf{N}\mathbf{B}^{-1} = \mathbf{W} \quad (\text{A.2})$$

Therefore a more optimum estimation of \mathbf{A} and \mathbf{B} can be achieved by minimizing the error function,

$$MSE = \text{trace}(\mathbf{W}^H\mathbf{W}) \quad (\text{A.3})$$

A fundamental ambiguity exists with the above approach. The problem is, given that \mathbf{A}' and \mathbf{B}' are solutions for \mathbf{A} and \mathbf{B} which minimize the MSE , then so are the solutions $\kappa\mathbf{A}'$ and $\kappa^{-1}\mathbf{B}'$. To remove this ambiguity, the complex gain coefficients are chosen so that

$$\text{imag}\{a_0\} = 0 \quad (\text{A.4})$$

and

$$\sum_{k=0}^{N-1} |a_i|^2 = N \quad (\text{A.5})$$

A closed form solution for determining \mathbf{A} and \mathbf{B} such that the MSE is minimized is unknown. The actual approach used to solve this problem was to minimize the MSE iteratively, first solving for \mathbf{A} only, then solving \mathbf{B} only, and repeating. The advantage of this approach is that the separate minimizations involved have closed form solutions. For

APPENDIX

each successive iteration, a_0, a_1, \dots, a_{N-1} can be solved using,

$$a'_i = \frac{\sum_{n=0}^{T-1} p_{in} p_{in}^*}{\sum_{n=0}^{T-1} s_{in} p_{in}^*} \quad (A.6)$$

for $0 \leq i \leq N - 1$ where a'_i is the unnormalized estimate of a_i , p_{in} and s_{in} are elements of the matrices \mathbf{P} and \mathbf{S} respectively, and

$$\mathbf{P} = \mathbf{X} \mathbf{B}^{-1} \quad (A.7)$$

The complex gain coefficients are then normalized so that

$$a_i = \frac{|a'_0| a'_i}{a'_0} \sqrt{\frac{N}{\sum_{i=0}^{N-1} |a'_i|^2}} \quad (A.8)$$

Similarly the parameters b_0, b_1, \dots, b_{T-1} can be solved each iteration using,

$$b_k = \frac{\sum_{m=0}^{N-1} q_{mk} q_{mk}^*}{\sum_{m=0}^{N-1} s_{mk} q_{mk}^*} \quad (A.9)$$

for $k = 0, 1, \dots, T - 1$ where q_{mk} is an element of the matrix \mathbf{Q} which is given by,

$$\mathbf{Q} = \mathbf{A}^{-1} \mathbf{X} \quad (A.10)$$

The minimization process is started by initializing the diagonal elements of \mathbf{B} according to

$$b_k = \sqrt{\mathbf{x}(t_k)^H \mathbf{x}(t_k)} \quad (A.11)$$

and then for each iteration, updating the elements of \mathbf{A} followed by the elements of \mathbf{B} , according to equations (A.6)–(A.10). Ten iterations was found to be more than enough to ensure the accuracy of the final estimates were sufficient for this report.

DOCUMENT CONTROL DATA

(Security classification of title, body of abstract and indexing annotation must be entered when the overall document is classified)

1. ORIGINATOR (the name and address of the organization preparing the document. Organizations for whom the document was prepared, e.g. Establishment sponsoring a contractor's report, or tasking agency, are entered in section 8.) DEFENCE RESEARCH ESTABLISHMENT OTTAWA NATIONAL DEFENCE SHIRLEYS BAY, OTTAWA, ONTARIO K1A 0K2 CANADA		2. SECURITY CLASSIFICATION (overall security classification of the document including special warning terms if applicable) UNCLASSIFIED
3. TITLE (the complete document title as indicated on the title page. Its classification should be indicated by the appropriate abbreviation (S,C or U) in parentheses after the title.) THE EFFECTS OF THE ENVIRONMENT ON AN EXPERIMENTAL VHF RADIO DIRECTION FINDING ANTENNA SYSTEM (U)		
4. AUTHORS (last name, first name, middle initial) READ, WILLIAM, J.L.		
5. DATE OF PUBLICATION (month and year of publication of document) AUGUST 1994	6a. NO. OF PAGES (total containing information. Include Annexes, Appendices, etc.) 71	6b. NO. OF REFS (total cited in document) 9
7. DESCRIPTIVE NOTES (the category of the document, e.g. technical report, technical note or memorandum. If appropriate, enter the type of report, e.g. interim, progress, summary, annual or final. Give the inclusive dates when a specific reporting period is covered.) DREO REPORT		
8. SPONSORING ACTIVITY (the name of the department project office or laboratory sponsoring the research and development. Include the address.) DEFENCE RESEARCH ESTABLISHMENT OTTAWA NATIONAL DEFENCE SHIRLEYS BAY, OTTAWA, ONTARIO K1A 0K2 CANADA		
9a. PROJECT OR GRANT NO. (if appropriate, the applicable research and development project or grant number under which the document was written. Please specify whether project or grant) 041LX	9b. CONTRACT NO. (if appropriate, the applicable number under which the document was written)	
10a. ORIGINATOR'S DOCUMENT NUMBER (the official document number by which the document is identified by the originating activity. This number must be unique to this document.) DREO REPORT 1226	10b. OTHER DOCUMENT NOS. (Any other numbers which may be assigned this document either by the originator or by the sponsor)	
11. DOCUMENT AVAILABILITY (any limitations on further dissemination of the document, other than those imposed by security classification) <input checked="" type="checkbox"/> Unlimited distribution <input type="checkbox"/> Distribution limited to defence departments and defence contractors; further distribution only as approved <input type="checkbox"/> Distribution limited to defence departments and Canadian defence contractors; further distribution only as approved <input type="checkbox"/> Distribution limited to government departments and agencies; further distribution only as approved <input type="checkbox"/> Distribution limited to defence departments; further distribution only as approved <input type="checkbox"/> Other (please specify):		
12. DOCUMENT ANNOUNCEMENT (any limitation to the bibliographic announcement of this document. This will normally correspond to the Document Availability (11). However, where further distribution (beyond the audience specified in 11) is possible, a wider announcement audience may be selected.) UNLIMITED		

UNCLASSIFIED

SECURITY CLASSIFICATION OF FORM

UNCLASSIFIED

SECURITY CLASSIFICATION OF FORM

13. ABSTRACT (a brief and factual summary of the document. It may also appear elsewhere in the body of the document itself. It is highly desirable that the abstract of classified documents be unclassified. Each paragraph of the abstract shall begin with an indication of the security classification of the information in the paragraph (unless the document itself is unclassified) represented as (S), (C), or (U). It is not necessary to include here abstracts in both official languages unless the text is bilingual).

(U) This report discusses the results of VHF radio direction finding (DF) experiments carried out with an experimental linear eight antenna DF system. The main purpose of these experiments was to investigate the effect of the environment, in particular multipath propagation, on DF performance. A theoretical analysis of all known error mechanisms has also been carried out in order to better understand the measured results. This includes temporal noise, equipment errors, mutual coupling, and multipath. The analysis of multipath also includes the development of new models to predict statistical effects. The results of this investigation indicate that multipath effects are complex and may create difficulties in modern systems if improved accuracy is an objective. Further measurements will be required to verify these preliminary findings.

14. KEYWORDS, DESCRIPTORS or IDENTIFIERS (technically meaningful terms or short phrases that characterize a document and could be helpful in cataloguing the document. They should be selected so that no security classification is required. Identifiers, such as equipment model designation, trade name, military project code name, geographic location may also be included. If possible keywords should be selected from a published thesaurus, e.g. Thesaurus of Engineering and Scientific Terms (TEST) and that thesaurus-identified. If it is not possible to select indexing terms which are Unclassified, the classification of each should be indicated as with the title.)

VHF
RADIO DIRECTION FINDING
ANTENNA ARRAYS
MULTIPATH
MUSIC
ARRAY CALIBRATION
MUTUAL COUPLING
DIRECTION OF ARRIVAL
MULTIPATH MODEL

UNCLASSIFIED

SECURITY CLASSIFICATION OF FORM